

# JGR Space Physics

## RESEARCH ARTICLE

10.1029/2021JA029475

### Key Points:

- Hemispheric asymmetry in auroral currents is larger for interplanetary magnetic field (IMF)  $B_y^+$  in the Northern Hemisphere (NH) ( $B_y^-$  in the Southern Hemisphere [SH]) than vice versa during both signs of IMF  $B_z$
- Strongest asymmetry occurs in local winter and autumn for  $B_y^+$  in the NH ( $B_y^-$  in the SH) and IMF  $B_z^+$  with NH/SH field aligned current ratio of about 1.18
- IMF  $B_y^+$  in the NH and  $B_y^-$  in the SH causes larger auroral currents than vice versa. Effect is stronger for IMF  $B_z^+$  than for IMF  $B_z^-$

### Correspondence to:

A. B. Workayehu,  
[abiyot.workayehu@oulu.fi](mailto:abiyot.workayehu@oulu.fi)

### Citation:

Workayehu, A. B., Vanhamäki, H., Aikio, A. T., & Shepherd, S. G. (2021). Effect of interplanetary magnetic field on hemispheric asymmetry in ionospheric horizontal and field-aligned currents during different seasons. *Journal of Geophysical Research: Space Physics*, 126, e2021JA029475. <https://doi.org/10.1029/2021JA029475>

Received 26 APR 2021  
Accepted 15 SEP 2021

## Effect of Interplanetary Magnetic Field on Hemispheric Asymmetry in Ionospheric Horizontal and Field-Aligned Currents During Different Seasons

A. B. Workayehu<sup>1</sup> , H. Vanhamäki<sup>1</sup> , A. T. Aikio<sup>1</sup> , and S. G. Shepherd<sup>2</sup> 

<sup>1</sup>Space Physics and Astronomy Research Unit, University of Oulu, Oulu, Finland, <sup>2</sup>Thayer School of Engineering, Dartmouth College, Hanover, NH, USA

**Abstract** We present a statistical investigation of the effects of interplanetary magnetic field (IMF) on hemispheric asymmetry in auroral currents. Nearly 6 years of magnetic field measurements from Swarm A and C satellites are analyzed. Bootstrap resampling is used to remove the difference in the number of samples and IMF conditions between the local seasons and the hemispheres. Currents are stronger in Northern Hemisphere (NH) than Southern Hemisphere (SH) for IMF  $B_y^+$  in NH ( $B_y^-$  in SH) in most local seasons under both signs of IMF  $B_z$ . For  $B_y^-$  in NH ( $B_y^+$  in SH), the hemispheric difference in currents is small except in local winter when currents in NH are stronger than in SH. During  $B_y^+$  and  $B_z^+$  in NH ( $B_y^-$  and  $B_z^+$  in SH), the largest hemispheric asymmetry occurs in local winter and autumn, when the NH/SH ratio of field aligned current (FAC) is  $1.18 \pm 0.09$  in winter and  $1.17 \pm 0.09$  in autumn. During  $B_y^+$  and  $B_z^-$  in NH ( $B_y^-$  and  $B_z^-$  in SH), the largest asymmetry is observed in local autumn with NH/SH ratio of  $1.16 \pm 0.07$  for FAC. We also find an explicit  $B_y$  effect on auroral currents in a given hemisphere: on average  $B_y^+$  in NH and  $B_y^-$  in SH causes larger currents than vice versa. The explicit  $B_y$  effect on divergence-free current during IMF  $B_z^+$  is in very good agreement with the  $B_y$  effect on the cross polar cap potential from the Super Dual Auroral Radar Network dynamic model except at SH equinox and NH summer.

## 1. Introduction

The effect of the interplanetary magnetic field (IMF) on the magnetosphere-ionosphere current systems is well documented (e.g., Juusola et al., 2014; Huang et al., 2017; Laundal et al., 2018; Milan et al., 2017; Reistad et al., 2014; Smith et al., 2017, and references therein). The southward IMF  $B_z$  (IMF  $B_z^-$ ) in the geocentric solar magnetospheric (GSM) reference frame causes an enhanced reconnection at the front of the magnetopause and allows a large amount of solar wind energy to enter into the Earth's magnetosphere, which subsequently increases the magnitudes of currents flowing in the coupled polar ionosphere. When the IMF  $B_z$  is northward (IMF  $B_z^+$ ), reconnection occurs at a location behind the cusps when the IMF draped over the magnetopause merges with the already opened tail lobe field lines (e.g., Burke & Doyle, 1986; Russell, 2000, and references therein). During this time, the amount of energy entering into the magnetosphere decreases and thus the intensity of currents in the polar ionosphere weaken. In addition to the IMF  $B_z$ , also the IMF  $B_x$ , and  $B_y$  components and solar wind velocity have an effect on the auroral currents. The auroral current system consists of both the field aligned currents (FACs) and ionospheric horizontal currents. The horizontal part of the auroral current system can further be divided into Pedersen and Hall currents which can in many situations be approximated by the curl-free (CF) and divergence-free (DF) horizontal current components, respectively.

The auroral current systems are related to the electric field that is imposed on the ionosphere by the ionosphere-magnetosphere coupling as well as IMF polarity (e.g., Cousins & Shepherd, 2010; Haaland et al., 2007; Pettigrew et al., 2010; Ruohoniemi & Greenwald, 2005; Thomas & Shepherd, 2018, and references therein). In most of these studies, the IMF  $B_y$  component is seen to rotate the average plasma convection patterns and electric field at the Northern Hemisphere (NH) and Southern Hemisphere (SH) in opposite directions, thereby creating asymmetry. Due to this, it is typical to compare the hemispheres during opposite IMF  $B_y$  polarity when addressing hemispheric asymmetry. Ruohoniemi and Greenwald (2005) have studied factors that influence the convection of plasma in the northern hemisphere high-latitude ionosphere. They found greater cross polar cap potential (CPCP) for IMF  $B_y^+$  than for  $B_y^-$  and more potential variation across

the dusk cell than the dawn cell. Using vector measurements of the electron drift velocity by the Electron Drift Instrument (EDI) on Cluster, Haaland et al. (2007) found larger cross polar cap potential for IMF  $B_y^+$  in the NH ( $B_y^-$  in the SH) than vice versa. Most recently, Thomas and Shepherd (2018) have found a linear increase in the cross polar cap potential with increasing  $K_p$  for a given IMF orientation at NH. Comparing  $B_y^+$  and  $B_y^-$  for each  $K_p < 5$ , the CPCP is always larger for  $B_y^+$  than for  $B_y^-$ . Pettigrew et al. (2010) have conducted a statistical study on the dipole tilt angle dependency and on the hemispheric symmetry of the high-latitude convection pattern and cross polar cap potential using Super Dual Auroral Radar Network (SuperDARN) measurements. They found larger CPCP in the NH than in the SH during IMF  $B_y^-$  in the NH ( $B_y^+$  in the SH) under neutral tilt (equinoxes).

Previous studies have reported the effect of IMF  $B_y$  on the geomagnetic activity and fluxes of high energy electron precipitation and (e.g., Holappa & Mursula, 2018; Holappa et al., 2020, 2021) and substorm occurrence rates (e.g., Liou et al., 2020; Ohma et al., 2021, and references therein). Holappa and Mursula (2018) and Holappa et al. (2021) found that, for a fixed value of solar wind coupling function, geomagnetic activity and large scale R1 and R2 FACs are stronger for IMF  $B_y^+$  than for IMF  $B_y^-$  in the NH winter, while in the SH winter the dependence on the  $B_y$  sign is reversed. Holappa et al. (2020) studied the explicit IMF  $B_y$  effect on the fluxes of high energy electron precipitation ( $>30$  keV) in the auroral region. They found larger precipitation fluxes for IMF  $B_y^+$  than IMF  $B_y^-$  in the NH winter (SH summer), and vice versa in NH summer (SH winter). Liou et al. (2020) investigated the effect of IMF  $B_y$  polarity on the substorm occurrence rate and found about 33% more substorms for  $B_y^+$  than for  $B_y^-$ . A recent study by Ohma et al. (2021) found that substorms occur more frequently when  $B_y$  and the dipole tilt angle have different signs as opposed to when they have the same sign. However, they did not find any clear evidence for any preference of stronger or more frequent substorm activity during  $B_y^+$  compared to  $B_y^-$ , and argued that the results by Liou et al. (2020) of a  $B_y^+$  preference were due to the choice of substorm list used.

Hemispheric asymmetry in auroral current systems has been reported in several previous studies (Coxon et al., 2016; Green et al., 2009; Huang et al., 2017; Laundal et al., 2016; Milan et al., 2017; Smith et al., 2017; Workayehu et al., 2019, 2020). Most of these studies reported larger average currents in the northern hemisphere (NH) than southern hemisphere (SH). In some studies the observed hemispheric difference was attributed to the satellite's orbital configuration (Green et al., 2009) or difference in the dayside reconnection (Coxon et al., 2016), while others raised data quality issues (Milan et al., 2017) and the role of data analysis methods (Laundal et al., 2017). Smith et al. (2017) have found a season-dependent hemispherical asymmetry in the auroral electrojet response to IMF  $B_y$ . When the hemispheres are compared under the same sign of  $B_y$ , they found stronger (weaker) currents in the NH than in the SH during  $B_y^+$  ( $B_y^-$ ) around the local winter. However, they did not find a significant IMF  $B_y$  effect on the auroral electrojet in the local summer season. Using Swarm magnetic field measurements Huang et al. (2017) found larger auroral electrojets in NH than in SH during local summer averaged over all IMF conditions. They also found that the prominent auroral electrojet currents are closely controlled by the solar wind energy input, but their intensity is not depend on IMF  $B_y$  orientation.

Very recently, Pakhotin et al. (2021), using Swarm A satellite data, studied electromagnetic energy input into the ionosphere by assessing the Poynting flux in the NH and SH. They found higher electromagnetic energy input into the NH than the SH even when averaged over season. They proposed that the observed hemispheric asymmetry in the electromagnetic energy input can be explained by the different solar illumination of the NH and SH auroral ovals.

Using Swarm A and C satellite data Workayehu et al. (2019), here after referred to as Paper I, examined hemispheric asymmetry in auroral currents during low ( $K_p < 2$ ) and high ( $K_p \geq 2$ ) geomagnetic activity conditions averaged over all local seasons. We found significant hemispheric asymmetry during low activity conditions, with about 10% more intense currents in NH than SH. Recently Workayehu et al. (2020), here after referred to as Paper II, studied the seasonal effect on FACs and horizontal currents using the same database as in Paper I with one extra year of data added. We found larger hemispheric asymmetry during low than high activity conditions, and during local winter and autumn seasons than during local spring and summer seasons, with more intense currents in NH than SH.

In this study, we present, to our knowledge, the first systematic study of IMF effect on the hemispheric asymmetry in the full auroral current system (FAC, CF, and DF current) during all seasons. This extends and complements the analysis carried out in Papers I and II by organizing the data according to IMF conditions, which is a necessary step in order to study the role of solar wind—magnetosphere coupling in the hemispheric asymmetry. Even though the main aim of the study is to study the hemispheric asymmetry in the auroral currents, we also investigated the explicit By effect in a given hemisphere. We use Swarm data during the time period April 15, 2014 to December 31, 2019, which is about 8 months more than in Paper II. We utilize the Spherical Elementary Current Systems (SECS) data analysis method (Amm et al., 2015; Juusola et al., 2016; Vanhamäki et al., 2020) like in Papers I and II.

The rest of the study is organized as follows: in Section 2, we briefly describe the data and data analysis methods including the bootstrap resampling method. In Section 3, we present the IMF dependence of FACs and ionospheric horizontal currents during different local seasons in NH and SH. In order to compare the hemispheric differences in the cross polar cap potential and associated electric field during different seasons, we calculate cross polar cap potential differences for different IMF orientations from the SuperDARN Dynamic Model (SDDM) (Cousins & Shepherd, 2010) in Section 4. Finally in Section 5, we present the summary and conclusions of the study.

## 2. Data Analysis

### 2.1. Swarm Data and SECS Analysis Method

The Swarm data set, magnetic field data analysis and coordinate systems used in the analysis were described in Paper I and II, and are briefly summarized here.

In this study, we utilize data measured by Swarm A and Swarm C satellites from April 15, 2014 to December 31, 2019. Specifically, we use the level-1b calibrated 1 Hz magnetic field data (the 0505 data set). For FAC and horizontal current estimation, we first obtain the variation magnetic field data by subtracting a background magnetic field model from the measured magnetic field data. We use CHAOS-6-x8 model for April 15, 2014–April 14, 2019 and CHAOS-7 for April 15–December 31, 2019. CHAOS model is a geomagnetic field model combining Earth's core, crust and magnetospheric currents (Finlay et al., 2016).

The Spherical Elementary Current Systems (SECS) method (Amm et al., 2015; Juusola et al., 2016; Vanhamäki et al., 2020; Workayehu et al., 2019) is used to estimate FAC and horizontal currents. For estimating currents using the Swarm/SECS analysis method, we first discard magnetic data poleward of  $\pm 80^\circ$  geographic latitude, where the longitudinal separation between Swarm A and C becomes too small for a reliable current estimation using this method. Locations of the satellite's magnetic footpoints and the vector magnetic field data are then converted to Spherical-AACGM (SPH-AACGM) coordinates (detailed description in Paper I).

The data from each orbit are divided into four overflights between ( $\pm 50^\circ$ ,  $\pm 80^\circ$ ) SPH-AACGM latitudes, and we discard that part of an overflight where the satellite path is nearly parallel to the SPH-AACGM latitudes (gradient of latitude is  $< 0.015^\circ/\text{s}$ ), since the analysis method fails in that situation. This condition is met more often in SH and most of the rejected points take place near  $80^\circ$  AACGM (Shepherd, 2014) latitude. Since we limit our analysis to SPH-AACGM latitudes lower than  $80^\circ$ , NH is very little affected by this rejection procedure and even in SH the effect on currents flowing within the oval is negligible (see Paper II for detailed description).

### 2.2. IMF and Solar Wind Data

In this study, we use the 1-min resolution IMF and solar wind OMNI data propagated to the Earth's bow shock. We average the OMNI data over 30-min period before oval crossings and then use the average values to calculate Newell solar wind coupling function  $d\Phi/dt$  (Newell et al., 2007).

To explore the effect of IMF on the hemispheric asymmetry in FACs and ionospheric horizontal currents during different local seasons, first we divide the oval crossings into four local seasons as we did in Paper II: NH spring and SH autumn ( $\pm 45$  days around March equinox), NH summer and SH winter ( $\pm 45$  days around June solstice), NH autumn and SH spring ( $\pm 45$  days around September equinox), and NH winter and SH

## Oval crossings as a function of coupling function

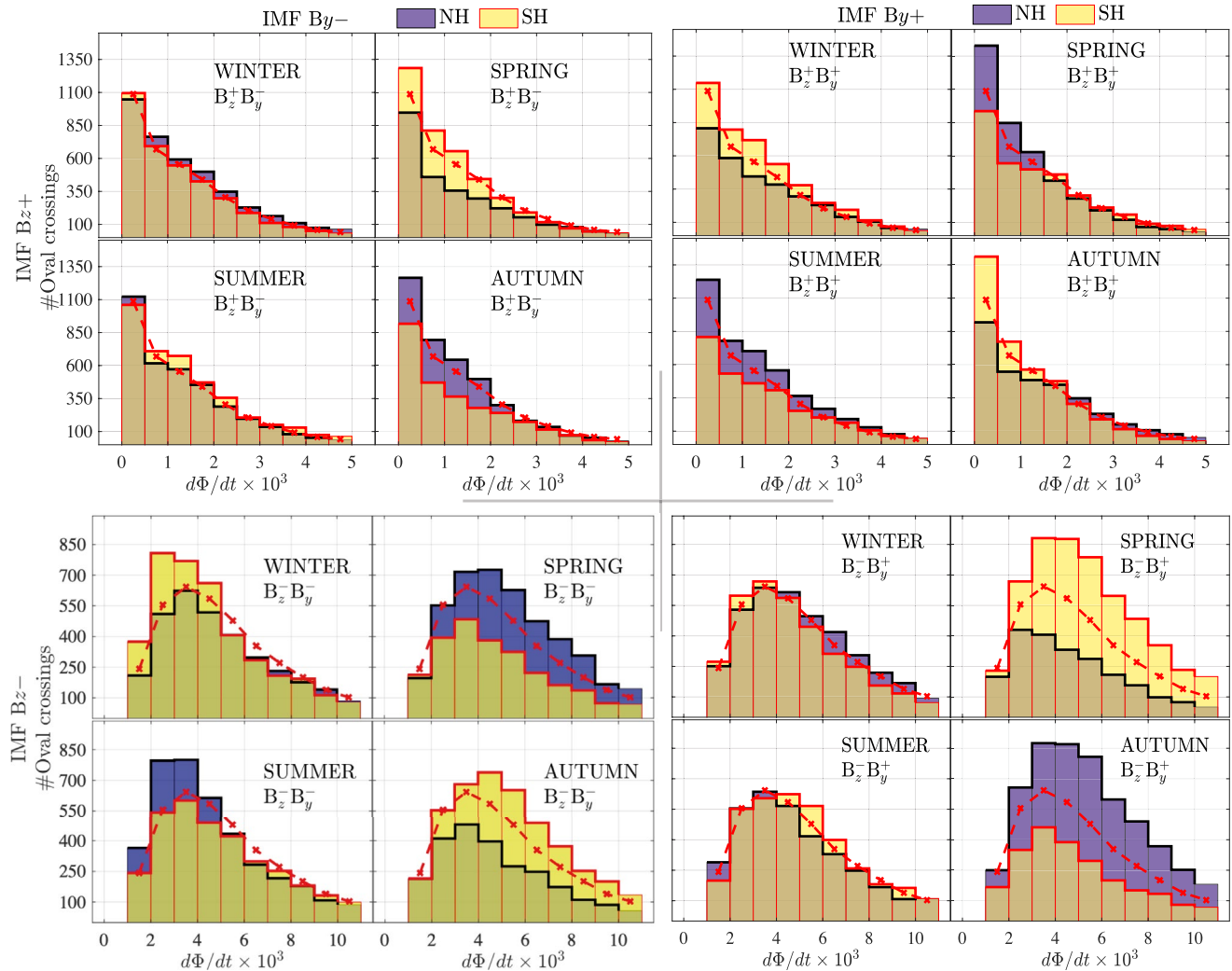


**Figure 1.** Distribution of Swarm oval crossings as function of Newell coupling function ( $d\Phi/dt$ ) for the four local seasons in the Northern (NH, blue) and Southern (SH, yellow) hemispheres. The distribution for each local season is sorted into four quadrants of IMF clock-angle:  $B_z^+B_y^-$ ,  $B_z^+B_y^+$ ,  $B_z^-B_y^+$  and  $B_z^-B_y^-$ , where the superscripts denote the positive and negative directions of interplanetary magnetic field  $B_z$  and  $B_y$  components. The red dashed line is the re-sampling (bootstrap) distribution of oval crossings. The blue and yellow distributions are for NH and SH, respectively.

summer ( $\pm 45$  days around December solstice). We further group the oval crossings in each local season into four IMF clock-angle sectors based on IMF  $B_y$  and  $B_z$  directions. Figure 1 shows the distribution of oval crossings as a function of values of the coupling function for the four local seasons and four clock-angle sectors in NH and SH. From now on, we will denote the positive and negative directions for each IMF component with superscripts. For IMF  $B_z^+$  conditions, the peak of the oval crossing distributions for all seasons is at the lowest bin, while for IMF  $B_z^-$  conditions the peak value locations are slightly different in the two hemispheres.

### 2.3. Bootstrapping by Using the Newell Coupling Function

From Figure 1, one can easily see the hemispheric differences in the coupling function distribution in each local season and IMF clock angle sectors. For example, in the  $B_z^-B_y^+$  sector during local spring, the number of oval crossings in SH is larger than in NH, while the difference is vice versa during local autumn. Similarly, a relatively large hemispheric difference is also seen during local spring and autumn seasons in the  $B_z^-B_y^-$  sector.

We correct for the hemispheric and seasonal differences in the Newell coupling function distributions by using bootstrap resampling (also known as bootstrapping). Bootstrapping is a statistical method that relies on random sampling with replacement from the original data (e.g., Chernick & LaBudde, 2011; Dekking et al., 2005). In this study, the original data are the Swarm oval crossings in each local season and each IMF clock angle sector. In order to re-sample from the original data, we first define sampling distribution (or bootstrap distribution) according to which we randomly take samples from the original data distribution. The sampling distribution is defined in such a way that the total number of Swarm oval crossings in each coupling function bin is the same for the four seasons and the two hemispheres, separately for IMF  $B_z^+$  and  $B_z^-$ . This way we get two sampling distributions, one for IMF  $B_z^+$  conditions and another for IMF  $B_z^-$  conditions, which are used for all seasons and IMF  $B_y$  directions. These are shown by the red dashed lines in Figure 1. For each local season and clock-angle sector, a total of 1,000 bootstrap samples are randomly taken with replacement from the original data. The numbers of oval crossings in each bootstrap sample are 3,595 and 3,571 for IMF  $B_z^+$  and  $B_z^-$  conditions, respectively, which are the average number of oval crossings in the original data set per season for each direction of IMF  $B_z$ . A similar method was used in Paper II to make the local seasons directly comparable to each other in terms of Kp index, but in this study our aim is to make the local seasons and IMF  $B_y$  polarity under the same IMF  $B_z$  direction directly comparable to each other.

The average ionospheric horizontal currents and FACs in each  $2^\circ$  AACGM latitude by 1 h MLT grid cells are calculated for each of the 1,000 bootstrap samples. The sizes of the grid cells in this study are larger than the sizes of the grid cells in Papers I and II, as now we divide the data in each local season into four IMF quadrants. From the 1,000 bootstrap samples, we have 1,000 different distributions of the average values. The median values of the average current densities in each grid cell are then calculated from the bootstrap statistics. These results, presented in Section 3, are our best estimates for the current densities in each grid cell.

### 3. Results

#### 3.1. Estimation of Total Currents

In Paper II, it was shown that the hemispheres are more asymmetric for low ( $K_p < 2$ ) than high ( $K_p \geq 2$ ) activity conditions, and in local winter and autumn when compared to local spring and summer seasons. Here we study how the IMF orientation affects the hemispheric asymmetry in auroral currents during different seasons.

In order to quantify the hemispheric differences in FACs and horizontal CF and DF currents, we calculate the total integrated FAC values, and the average horizontal CF and DF currents for the four IMF clock angle sectors during each local season and IMF direction using the same formula as in Papers I and II, summarized below.

The total integrated FAC flowing between  $(60^\circ, 80^\circ)$  AACGM latitudes and all MLTs is obtained by

$$I = \sum_{m=1}^M |\text{FAC}_m| S_m, \quad (1)$$

where  $\text{FAC}_m$  is the FAC density in grid cell  $m$ ,  $S_m$  is the physical grid cell area calculated by converting the AACGM grid cell (MLT vs. AACGM latitude) to geographical coordinate system, and  $M$  is the total number of grid cells. The integrated FAC values contain contributions both from the upward and downward FACs.

For the CF and DF currents, we first calculate the magnitude of the current density in each grid cell as the square root of the sum of the squares of meridional (positive southward) and zonal (positive eastward) current density components. The average CF and DF current values between  $(60^\circ, 80^\circ)$  are then calculated between  $(60^\circ, 80^\circ)$  AACGM latitudes over all MLTs using the formula

$$I = \frac{1}{M} \sum_{m=1}^M \Delta_{m,\phi} \sqrt{J_{m,\phi}^2 + J_{m,\theta}^2}, \quad (2)$$

where  $J_{m,\theta}$  and  $J_{m,\phi}$  are the meridional and zonal current density components in grid cell  $m$ , respectively,  $M$  is the total number of grid cells between  $(60^\circ, 80^\circ)$  AACGM latitudes and over all MLTs, while  $\Delta_{m,\phi}$  is the zonal dimension of the grid cell calculated by converting the AACGM grid cell (MLT vs. AACGM latitude) to geographical coordinate system.



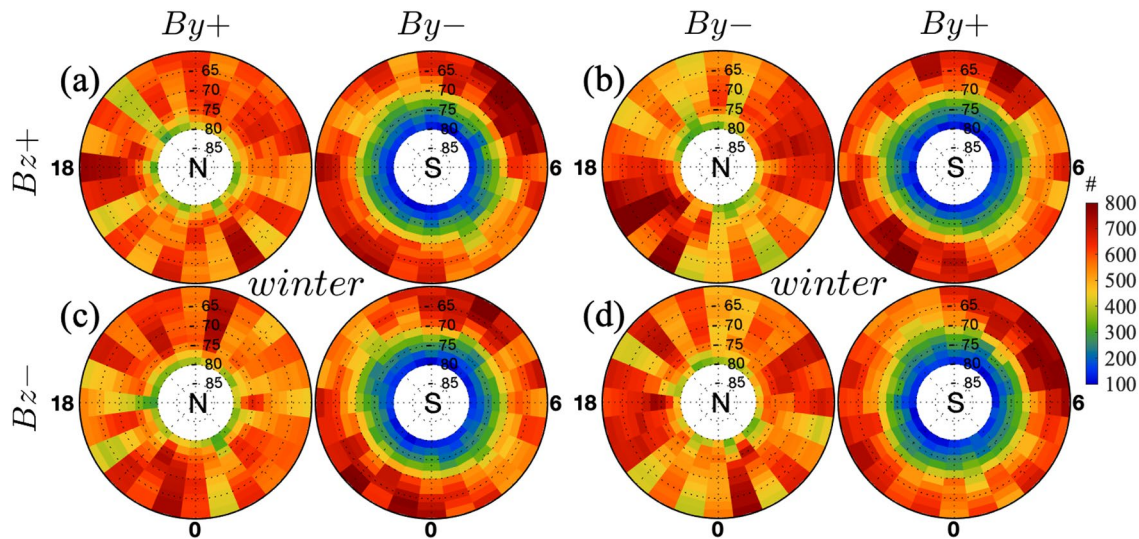


**Figure 2.** Distribution of the number of data points after bootstrapping in local winter for the four interplanetary magnetic field clock angle sectors in Northern Hemisphere and Southern Hemisphere. The plots are given in AACGM latitude by MLT. For both hemispheres, the noon (12 MLT) is at the top and evening (18 MLT) is at the left and the lowest latitude is  $60^\circ$ .

Figure 2 shows distributions of the number of data points after bootstrapping in the two hemispheres for the local winter season. Other seasons (not shown here) have similar distributions. The bootstrapping equalizes the total number of data points between the two hemispheres in each local season and IMF clock angle sector (see Figure 1), while Figure 2 shows how the data after bootstrapping are distributed spatially. In each IMF  $B_z$  direction, the NH and SH have distributions for opposite IMF  $B_y$  next to each other. When we compare the hemispheres with each other in the subsequent sections, we select the IMF  $B_y$  direction in NH and use the opposite IMF  $B_y$  sign in SH. This selection is necessary because the IMF  $B_y$  rotates the ionospheric convection pattern in opposite directions in the two hemispheres (see e.g., Figure 8 in Pettigrew et al., 2010). In all IMF sectors the NH has more data points than the SH poleward of  $\pm 66^\circ$  AACGM latitude, while the SH has more samples between  $60^\circ$  and  $65^\circ$  AACGM latitudes. This is due to the difference in the locations of AACGM poles relative to the geographic poles in the two hemispheres and the Swarm A and C satellites' near polar orbits (see Figure 1 in Paper I).

### 3.2. IMF Effect on Current Distributions in Both Hemispheres

In this section, we present the effect of IMF  $B_y$  direction on the magnitude and distributions of currents during each local season under northward and southward IMF  $B_z$ . In order to see the influence of IMF  $B_y$  on FACs, CF, and DF currents during each local season more clearly, we calculate the ratios of the total integrated currents between the two IMF  $B_y$  directions for each hemisphere.

Figure 3 shows distributions of median FACs, CF and DF current densities obtained with bootstrapping in both hemispheres during local winter. As expected, stronger FACs (Figures 3a–3d) occur during IMF  $B_z^-$  than IMF  $B_z^+$  for both hemispheres and IMF  $B_y$  signs (note the difference in color scales). Comparison of FACs during IMF  $B_y^{+/-}$  in each hemisphere separately indicates that the sign of  $B_y$  affects the magnitude and spatial distribution of FACs. In NH, FAC density during  $B_y^+$  seems to be larger than during  $B_y^-$  conditions while in SH, FAC density during  $B_y^-$  seems to be larger than during  $B_y^+$  conditions. In both hemispheres, strong median FACs occur in the premidnight MLT sector between 19–24 MLTs during all IMF clock angle sectors. This enhancement of FAC on the premidnight MLT sector during local winter season is in line with previous results reported by (e.g., Ohtani et al., 2005; Workayehu et al., 2020, and references)

Figure 3 shows also distributions of median CF (panels e–h) and median DF (panels i–l) current densities (both magnitude and vectors). In each hemisphere, the median CF and DF currents show generally similar IMF dependence as FACs: stronger median currents during IMF  $B_z^-$  than during IMF  $B_z^+$  conditions, and during  $B_y^+$  than  $B_y^-$  conditions in the NH (opposite IMF  $B_y$  sign in the SH). A more close comparison of

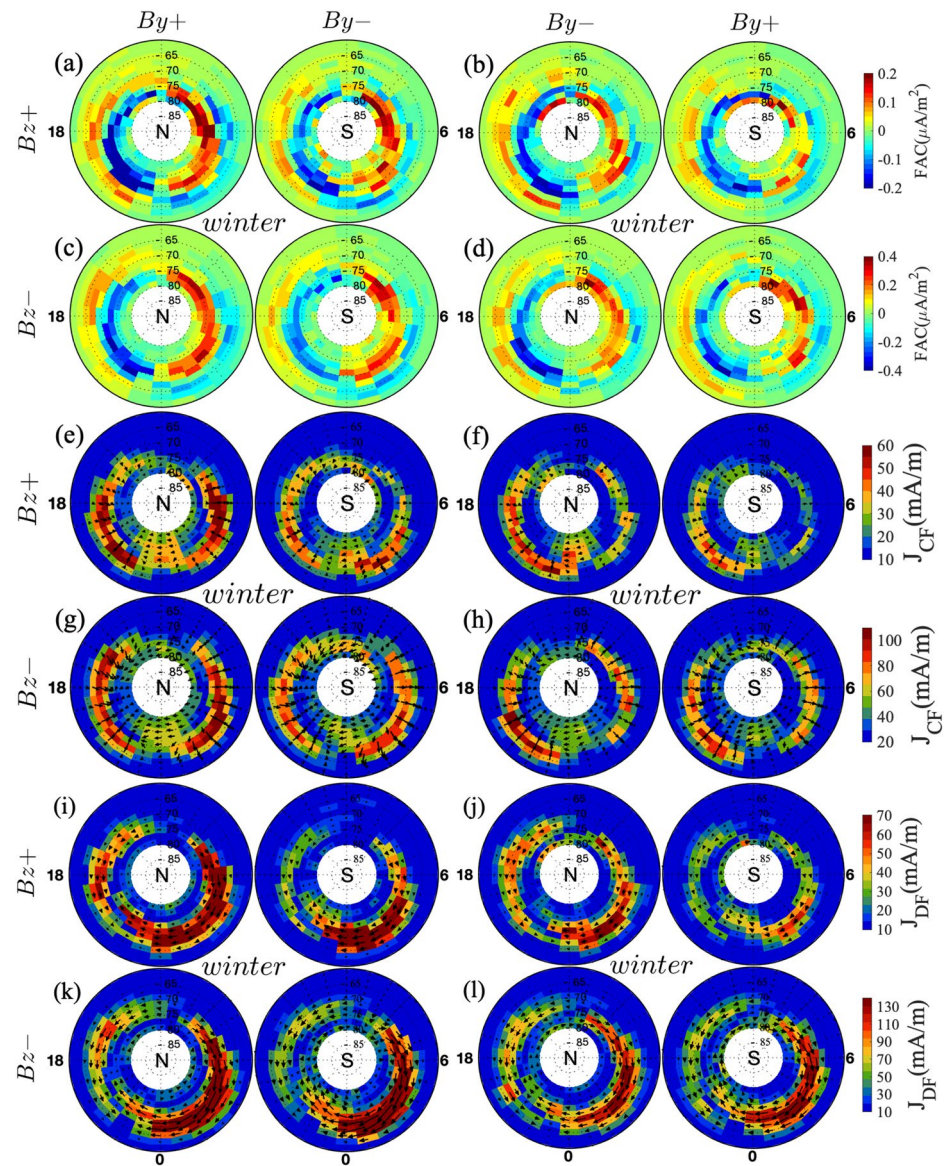


**Figure 3.** Distributions of median field aligned current (FAC) density (a–d), median CF current density (e–h) and median DF current density (i–l) in local winter for the four interplanetary magnetic field (IMF) clock angles in Northern Hemisphere (NH) and Southern Hemisphere (SH). Downward (upward) FACs are defined as positive (negative). The magnitudes and flow directions of median CF and DF currents are shown in color and arrows, respectively. From left to right: the first and second columns are for  $B_y^+$  in the NH and for  $B_y^-$  in the SH, and the third and fourth columns are for  $B_y^-$  in the NH and for  $B_y^+$  in the SH, respectively. From top to bottom: the first, third and fifth rows are for  $B_z^+$ , while the second, fourth and sixth rows are for  $B_z^-$ . The plots are given in AACGM latitude by MLT. For both hemispheres, the noon (12 MLT) is at the top and evening (18 MLT) is at the left and the lowest latitude is 60°. Note that the color scales for currents during IMF  $B_z^+$  and  $B_z^-$  conditions are different.

median CF currents between the two IMF  $B_y$  signs in each hemisphere indicates that the cross polar cap CF current is larger for IMF  $B_y^+$  in the NH ( $B_y^-$  in the SH) during both IMF  $B_z$  conditions. This result is consistent with the stronger dawn side R1 FACs shown in Figures 3a and 3c. The eastward and westward flowing DF currents (see Figures 3i–3l) display the well-known eastward and westward electrojets, EEJ and WEJ, respectively. For all IMF sectors, the WEJ currents are stronger than the EEJ currents in both hemispheres. The WEJ current densities are stronger for IMF  $B_y^+$  in the NH ( $B_y^-$  in the SH) than vice versa during both IMF  $B_z$  directions. Furthermore, the Harang discontinuity region, which is an overlap between EEJ and WEJ in the premidnight MLT sector with sharp latitudinal separation, occurs during all IMF sectors. This



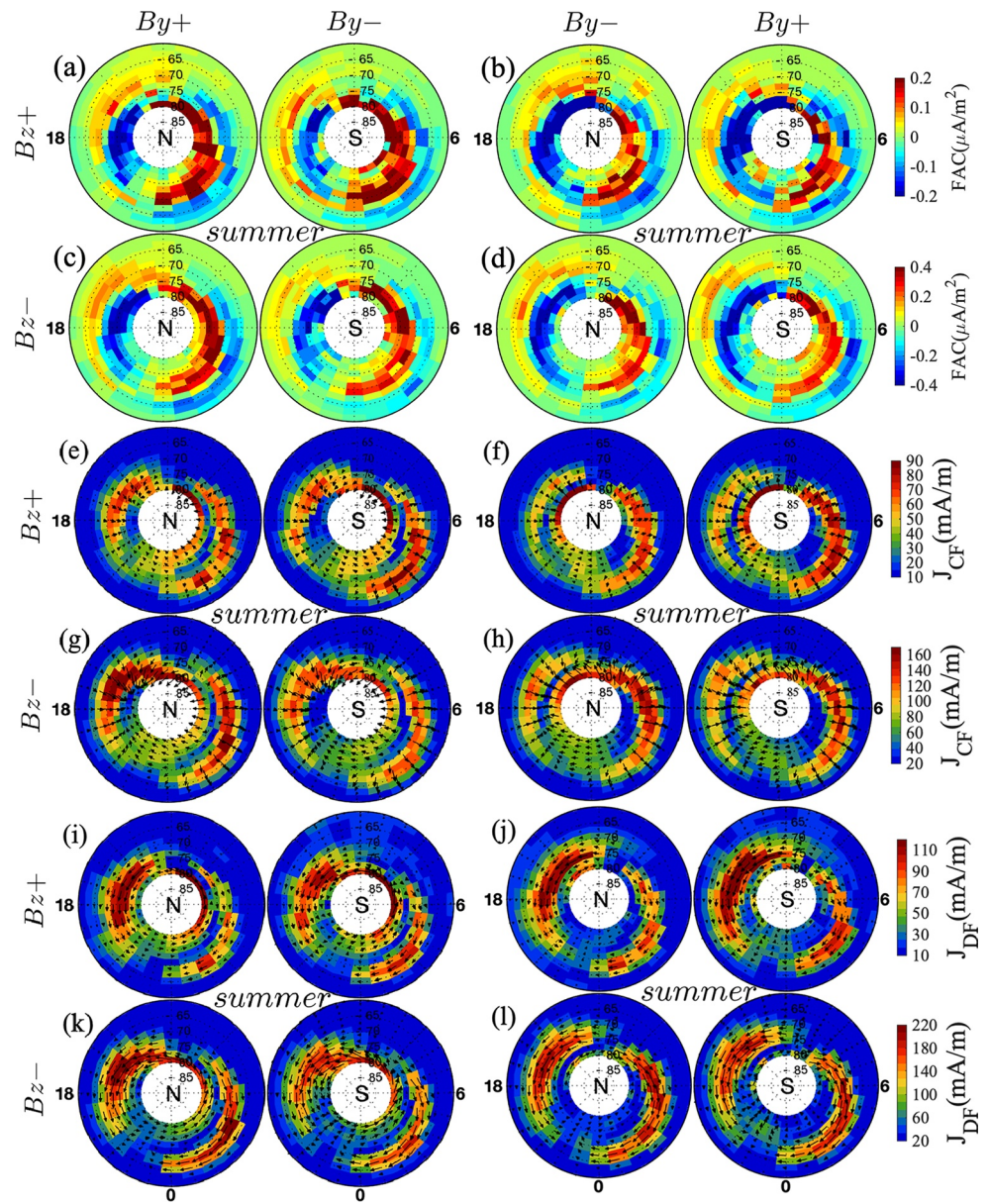


**Figure 4.** Same format as Figure 3, but for local summer.

is in line with the result in Paper II, and here our result indicates that the IMF  $B_y$  sign doesn't affect the occurrence of Harang discontinuity during local winter.

Figure 4 shows distributions of the median current densities during local summer in the same format as Figure 3. Figures 4a–4d indicate that the post-noon and dusk (12–19 MLT) R1 FACs are stronger and flow in a wide range of MLTs when IMF  $B_y$  is negative in NH (Figures 4b and 4d) than when it is positive (Figures 4a and 4c). Conversely, the dawnside R1 FACs seem to be stronger when IMF  $B_y$  is positive in NH than vice versa. The median CF current distributions (Figures 4e–4h) show similar dawn/dusk imbalance with IMF  $B_y$  direction as the median FACs, but the effect of IMF  $B_y$  direction on the median DF current (Figures 4i–4l) seems smaller. However, a closer look to the WEJ indicates a tendency of stronger WEJ current for IMF  $B_y^-$  in the NH ( $B_y^+$  in the SH) than vice versa. This is opposite to the IMF  $B_y$  on WEJ current during local winter. Comparison of the AACGM latitude by MLT distributions of currents during local winter and summer (see Figures 3 and 4) in each hemisphere shows the well known winter-summer difference in the magnitudes of currents irrespective of the IMF directions. This effect is obviously associated with



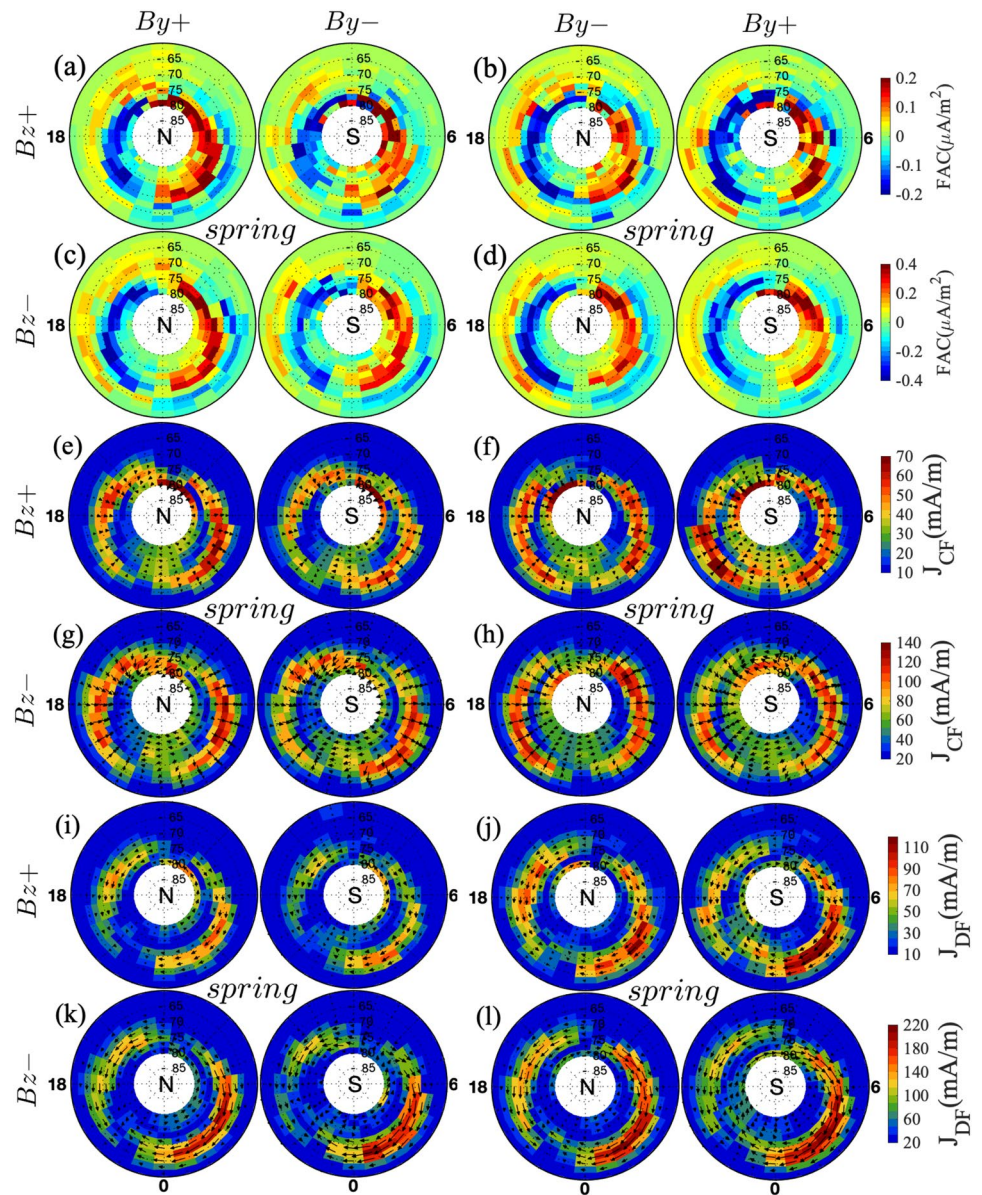


**Figure 5.** Same format as Figure 3, but for local spring.

the winter-summer difference in the background ionospheric conductances due to solar illumination (see also Section 3 in Paper II). At the auroral oval and polar cap, solar induced ionospheric conductances are larger in local summer than in local winter, and due to this stronger CF currents flowing from dawn to dusk and return DF currents occur during local summer (see Laundal et al., 2016 for further discussion). When comparing current distributions in winter and summer at the premidnight MLT sector, there is the Harang discontinuity difference which we saw already in Paper II: The EEJ and WEJ are separated latitudinally during local winter and longitudinally during local summer.

Figures 5a–5l show distributions of currents in NH and SH for different IMF sectors during local spring. Like in local summer, the post-noon and dusk R1 FAC seems stronger and flows in a wide range of MLTs when  $B_y$  is negative in NH (Figures 5b and 5d) than when it is positive (Figures 5a and 5c) for IMF  $B_z^+$ . Distributions of median CF currents (Figures 5e–5h) show similar IMF  $B_y$  dependence as FACs. Unlike FACs and CF currents, distributions of DF currents (Figures 5i–5l) indicate that both EEJ and WEJ currents are stronger for IMF  $B_y^-$  in the NH ( $B_y^+$  in the SH) than vice versa.

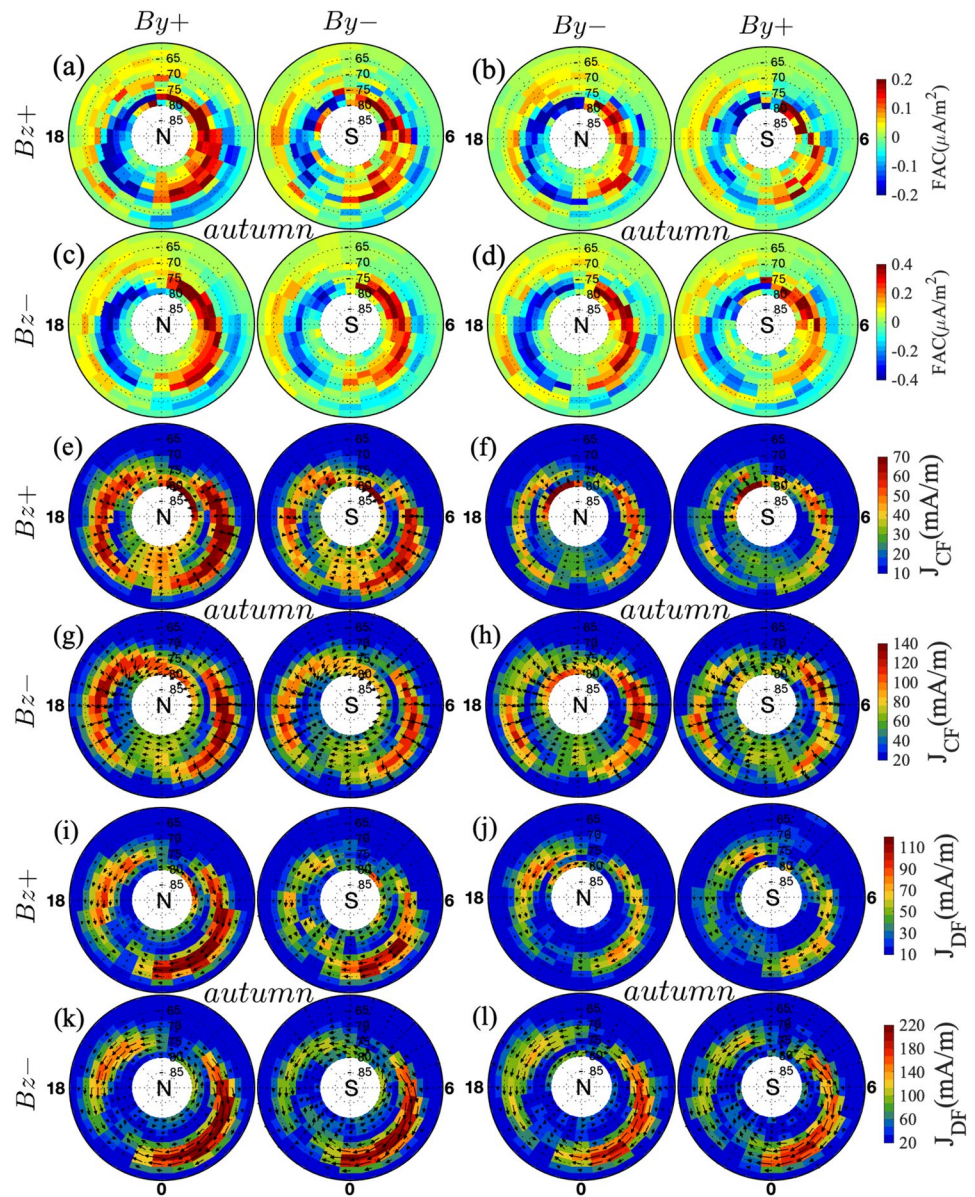


**Figure 6.** Same format as Figure 3, but for local autumn.

Figures 6a–6l show distributions of median FACs (Figures 6a–6d), median CF currents (Figures 6e–6h), and median DF currents (Figures 6i–6l) in NH and SH for different IMF sectors during local autumn. The FAC and CF current densities are stronger when  $B_y$  is positive in NH (negative in SH) than vice versa. Unlike for local spring, but like for local winter, both the EEJ and WEJ currents are larger for  $B_y^+$  in the NH ( $B_y^-$  in the SH) than vice versa during both IMF  $B_z$  directions.

The results indicate that the IMF  $B_y$  has strong influence on auroral current systems in both hemispheres, but this influence depends on the local season and IMF  $B_z$  direction. In Table 1, we show ratios of currents for opposite IMF  $B_y$  directions in each hemisphere separately during both IMF  $B_z$  conditions. In NH (Table 1a) during IMF  $B_z^+$  conditions, the largest IMF  $B_y$  effect on ionospheric currents occurs in local winter and autumn. In NH winter all the current components (FAC, CF, and DF) are about 20%–35% larger for IMF  $B_y^+$  than  $B_y^-$ , while in autumn the effect is even larger, about 35%–70%. In contrast, during NH spring and NH summer the effect is much smaller. Similar IMF  $B_y$  effect and seasonal pattern is visible also during IMF  $B_z^-$  conditions, but the effect is smaller, with the maximum enhancement of 15%–20% during winter.



**Table 1**

Ratios of Integrated Currents for Opposite IMF By Directions in Each Hemisphere:  $By^+/By^-$  in NH (a) and  $By^-/By^+$  in SH (b)

(a) Integrated current ratios for opposite IMF By directions in NH: $By^+/By^-$					
IMF	Currents	Winter	Spring	Autumn	Summer
$Bz^+$	FAC	$1.21 \pm 0.09$	$0.98 \pm 0.07$	$1.36 \pm 0.09$	$1.01 \pm 0.07$
	$I_{CF}$	$1.35 \pm 0.07$	$1.00 \pm 0.04$	$1.73 \pm 0.08$	$1.12 \pm 0.04$
	$I_{DF}$	$1.18 \pm 0.07$	$0.76 \pm 0.04$	$1.53 \pm 0.07$	$0.98 \pm 0.03$
$Bz^-$	FAC	$1.15 \pm 0.07$	$1.02 \pm 0.06$	$1.10 \pm 0.06$	$1.12 \pm 0.06$
	$I_{CF}$	$1.26 \pm 0.04$	$1.07 \pm 0.03$	$1.18 \pm 0.04$	$1.06 \pm 0.02$
	$I_{DF}$	$1.15 \pm 0.04$	$0.93 \pm 0.03$	$1.12 \pm 0.04$	$1.03 \pm 0.03$
(b) Integrated current ratios for opposite IMF By directions in SH: $By^-/By^+$					
IMF	Currents	Winter	Spring	Autumn	Summer
$Bz^+$	FAC	$1.14 \pm 0.09$	$0.84 \pm 0.07$	$1.17 \pm 0.09$	$0.99 \pm 0.08$
	$I_{CF}$	$1.36 \pm 0.08$	$0.83 \pm 0.04$	$1.45 \pm 0.08$	$1.07 \pm 0.05$
	$I_{DF}$	$1.31 \pm 0.08$	$0.68 \pm 0.04$	$1.34 \pm 0.07$	$0.96 \pm 0.04$
$Bz^-$	FAC	$1.04 \pm 0.08$	$1.01 \pm 0.07$	$1.01 \pm 0.07$	$0.95 \pm 0.06$
	$I_{CF}$	$1.24 \pm 0.04$	$1.01 \pm 0.03$	$1.12 \pm 0.04$	$1.00 \pm 0.03$
	$I_{DF}$	$1.13 \pm 0.05$	$0.84 \pm 0.03$	$1.07 \pm 0.06$	$1.03 \pm 0.04$

Note. IMF, interplanetary magnetic field; NH, Northern Hemisphere; SH, Southern Hemisphere.

Table 1b shows the IMF By effect in SH, but with the By signs switched. The seasonal and IMF  $Bz$  variations are similar to the NH, with the IMF By effect being larger during IMF  $Bz^+$  and local winter and autumn. In contrast to NH, a large effect is also seen in local spring during IMF  $Bz^+$  conditions, when the currents are 25%–30% smaller for IMF  $By^-$  than for IMF  $By^+$ .

Overall, the IMF By effect tends to be stronger during IMF  $Bz^+$  than IMF  $Bz^-$  conditions in both hemispheres. This is in line with Smith et al. (2017) results, even though they did not consider different seasons separately under different IMF conditions. Averaged over all seasons in NH, they found about 11% and 7% stronger auroral electrojet currents during IMF  $Bz^+$  and IMF  $Bz^-$ , respectively, when IMF By is positive than when it is negative. However, they did not find a significant IMF By sign effect on the auroral electrojet current in SH during either IMF  $Bz$  direction, which is contrary to our finding.

### 3.3. IMF Effect on Hemispheric Asymmetry in Currents

Visual inspection of Figures 3–6 shows that IMF By affects the hemispheric asymmetry between NH and SH. In this section, we compare currents from the two hemispheres in terms of integrated current values and corresponding NH/SH ratios during each local season under opposite IMF By directions.

Figure 7 and Table 2a quantify the magnitudes of currents and NH/SH ratios during IMF  $Bz^+$  in NH and SH under opposite IMF By directions. Figures 7a and 7b show the seasonal variations of integrated FACs when the sign of By in NH is positive and negative, respectively. The error bars are the 90% confidence ranges obtained from bootstrapping. For  $By^+$  in the NH (Figure 7a), hemispheric difference in FAC occurs in local winter and local autumn, when the integrated FAC is larger in NH than in SH. In contrast, during local spring and local summer the currents in the two hemispheres are equal within the confidence limits. In each hemisphere, comparison of the integrated FAC values during the equinoxes indicate a tendency of larger currents flowing during local autumn than spring, although in SH the effect is not statistically significant.

For  $By^-$  in the NH (Figure 7b), the seasonal behavior is very different. The integrated FAC increases from local winter to spring and then decreases in local autumn and again reaches its peak value in local summer. Comparison of Figures 7a and 7b shows that IMF By has a strong effect on the seasonal variations of FAC



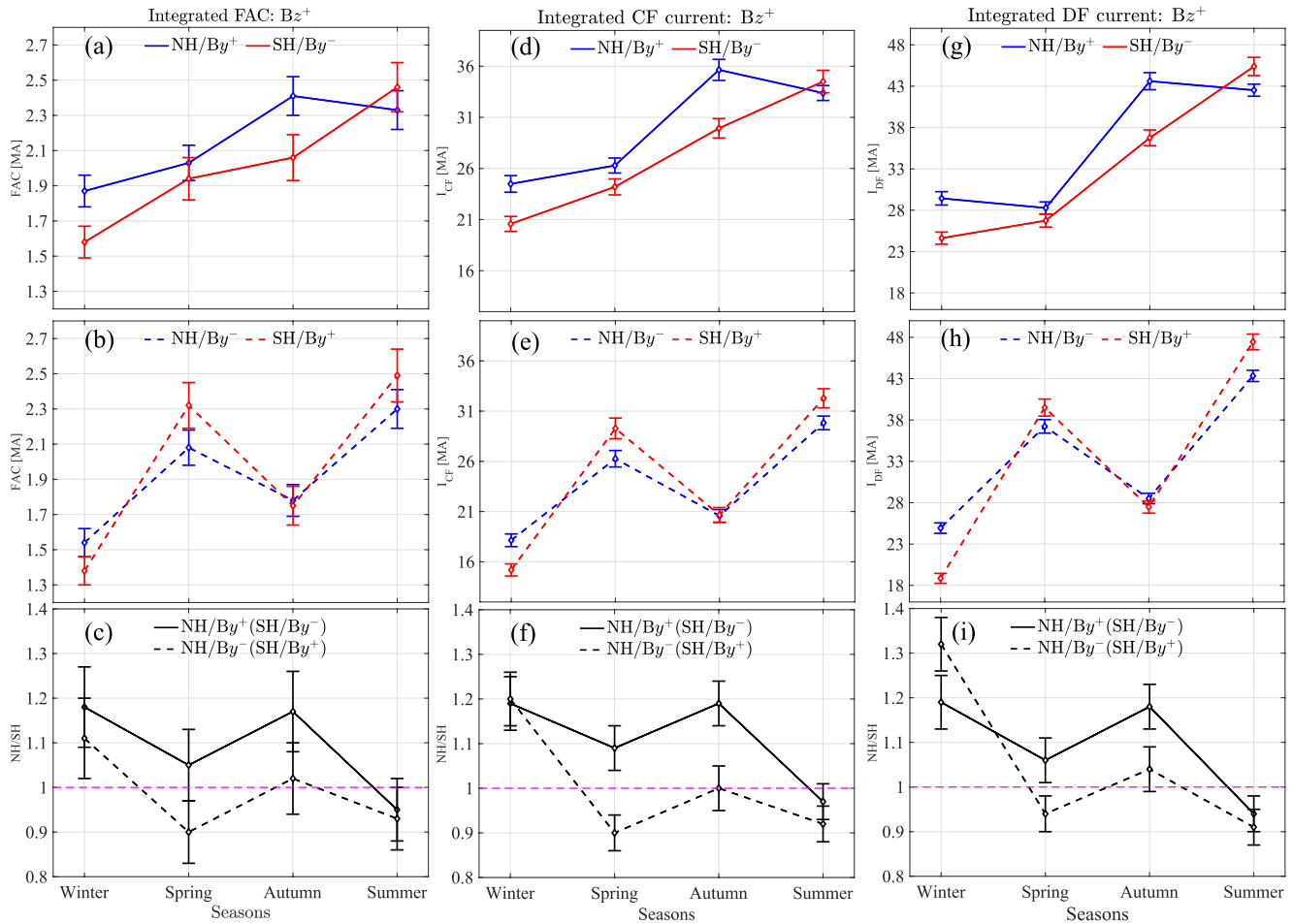


**Figure 7.** Median values of integrated field aligned current (FAC; panels: a–b), average CF (panels: d–e), and average DF (panels: g–h) currents as a function of season for interplanetary magnetic field (IMF)  $B_z^+$  and opposite IMF  $B_y$  directions in Northern Hemisphere (NH) and Southern Hemisphere (SH). The bottom panels are the median NH/SH ratios of FAC (c), CF current (f) and DF current (i). The error bars are the 90% confidence ranges.

during IMF  $B_z^+$ , especially during the equinoxes. In NH the integrated FAC is larger in autumn than in spring during  $B_y^+$ , and vice versa during  $B_y^-$ . In SH the  $B_y$  effect is opposite.

Figure 7c shows the seasonal variation of the median NH/SH ratios of FACs obtained from bootstrapping for opposite IMF  $B_y$  directions in the two hemispheres during IMF  $B_z^+$ . As these ratios are calculated for each bootstrap sample separately, the values in Figure 7c are not the ratios of the median values shown in Figures 7a and 7b, but in practice the difference is very small. For  $B_y^+$  in the NH (solid line, corresponds to Figure 7a), statistically significant asymmetry occurs in local winter and autumn with the NH/SH ratios  $1.18 \pm 0.09$  and  $1.17 \pm 0.09$ , respectively (see Table 2a). For  $B_y^-$  conditions in the NH (dashed line, corresponding to Figure 7b), statistically significant hemispheric asymmetry occurs during local winter and spring, when the NH/SH ratios are  $1.11 \pm 0.06$  and  $0.90 \pm 0.07$ , respectively.

Figures 7d, 7e, 7g and 7h, quantify the seasonal variation of average CF and DF currents, respectively, during IMF  $B_z^+$  conditions. For both IMF  $B_y$  signs, the seasonal pattern of average CF and DF currents are very similar to integrated FACs. For  $B_y^+$  in the NH (solid lines in Figures 7d and 7f), the largest hemispheric asymmetry occurs in local winter and local autumn, when the NH/SH ratios are  $1.19 \pm 0.06$  and  $1.19 \pm 0.05$  for CF currents, and  $1.19 \pm 0.07$  and  $1.18 \pm 0.06$  for DF currents (see Table 2a). Similarly, for  $B_y^-$  in the NH (dashed lines), the largest asymmetry takes place in local winter, with NH/SH ratios of  $1.20 \pm 0.07$  for CF and  $1.32 \pm 0.08$  for DF currents (see Table 2a). In addition, statistically significant hemispheric asymmetry occurs in local spring and local summer, with larger currents flowing in SH than in NH. Like for FACs, CF and DF currents are larger in autumn than in spring for  $B_y^+$  in the NH ( $B_y^-$  in the SH) and vice versa for

**Table 2**NH/SH Ratios of Integrated Currents for Opposite IMF By Directions: During IMF  $B_z^+$  (a, Same as in Figure 7) and During IMF  $B_z^-$  (b, Same as in Figure 8)

(a) NH/SH ratios of currents for opposite IMF By direction during IMF $B_z^+$					
IMF By	Currents	Winter	Spring	Autumn	Summer
$By^+$ NH ( $By^-$ SH)	FAC	$1.18 \pm 0.09$	$1.05 \pm 0.08$	$1.17 \pm 0.09$	$0.95 \pm 0.07$
	$I_{CF}$	$1.19 \pm 0.06$	$1.09 \pm 0.05$	$1.19 \pm 0.05$	$0.97 \pm 0.04$
	$I_{DF}$	$1.19 \pm 0.07$	$1.06 \pm 0.06$	$1.18 \pm 0.06$	$0.94 \pm 0.04$
$By^-$ NH ( $By^+$ SH)	FAC	$1.11 \pm 0.09$	$0.90 \pm 0.07$	$1.02 \pm 0.08$	$0.93 \pm 0.07$
	$I_{CF}$	$1.20 \pm 0.07$	$0.90 \pm 0.04$	$1.00 \pm 0.05$	$0.92 \pm 0.04$
	$I_{DF}$	$1.32 \pm 0.08$	$0.94 \pm 0.05$	$1.04 \pm 0.05$	$0.91 \pm 0.03$
(b) NH/SH ratios of currents for opposite IMF By direction during IMF $B_z^-$					
IMF By	Currents	Winter	Spring	Autumn	Summer
$By^+$ NH ( $By^-$ SH)	FAC	$1.11 \pm 0.09$	$0.90 \pm 0.07$	$1.02 \pm 0.08$	$0.93 \pm 0.07$
	$I_{CF}$	$1.06 \pm 0.04$	$1.04 \pm 0.04$	$1.15 \pm 0.03$	$1.10 \pm 0.03$
	$I_{DF}$	$1.02 \pm 0.04$	$1.05 \pm 0.04$	$1.13 \pm 0.04$	$1.07 \pm 0.03$
$By^-$ NH ( $By^+$ SH)	FAC	$0.98 \pm 0.07$	$1.05 \pm 0.07$	$1.06 \pm 0.07$	$0.94 \pm 0.06$
	$I_{CF}$	$1.05 \pm 0.04$	$0.99 \pm 0.03$	$1.09 \pm 0.04$	$1.03 \pm 0.03$
	$I_{DF}$	$1.01 \pm 0.04$	$0.95 \pm 0.03$	$1.08 \pm 0.04$	$1.00 \pm 0.03$

Note. For both IMF  $B_z$  conditions, the values in the first and second rows are for  $By^+$  in the NH ( $By^-$  in the SH) and for  $By^-$  in the NH ( $By^+$  in the SH), respectively. IMF, interplanetary magnetic field; NH, Northern Hemisphere; SH, Southern Hemisphere.

$By^-$  in the NH ( $By^+$  in the SH). The observed spring-autumn asymmetry in currents may be related to the Russell-McPherron (RM) effect (Russell & McPherron, 1973). It is a geometrical projection effect between the geocentric solar equatorial (GSEQ) and GSM coordinate systems that increases the likelihood of southward IMF  $B_z$  (in the GSM system) if IMF  $By$  is positive in the fall or negative in the spring (e.g., Lockwood et al., 2020; Zhao & Zong, 2012). Even though the bootstrapping method should remove the RM effect, we see that for IMF  $B_z^+$ , the spring currents are stronger than autumn currents for  $By^-$  in the NH and vice versa for  $By^+$  (Figure 7), which still follows the expected RM effect. The reason for this difference is at present unclear, but it could be related to the leakage of the RM effect to the results by using the Newell coupling function for bootstrapping or by the memory of the M-I system. We use 30-min averages for the coupling function and hence if there is a memory, solar wind forcing prior to the 30 min interval could still have an effect.

Another known factor contributing to the observed spring-autumn asymmetry in currents may be related to the spring-fall asymmetry in the amplitude of global geomagnetic activity reported in previous studies (e.g., Mursula et al., 2011, references therein). Mursula et al. (2011) found maxima of Ap index alternating between spring and fall during the declining phases of two consecutive solar cycles 22 and 23, which they attributed to alternating hemispheric asymmetry in the Sun. Our data set is taken entirely from the declining phase of solar cycle 24, so it could be expected that the spring-autumn asymmetry in currents flips the other way in the next (or previous) solar cycle.

Figure 8 and Table 2b show the integrated currents and hemispheric ratios for IMF  $B_z^-$  conditions, in the same format as Figure 7. When IMF  $By$  is positive in NH (Figure 8a), the smallest and largest integrated FAC occur in local winter and local summer, respectively, with the values in local spring and local autumn somewhere in between. Hemispheric difference occurs in local autumn and in local summer, with stronger currents flowing in NH than in SH. Similarly, when IMF  $By$  is negative in NH (Figure 8b), the smallest and largest integrated FAC occur in local winter and local summer, respectively. Unlike during IMF  $B_z^+$  conditions shown in Figure 7b, the FAC values in local spring and local autumn are equal within the 90% confidence ranges in each hemisphere.

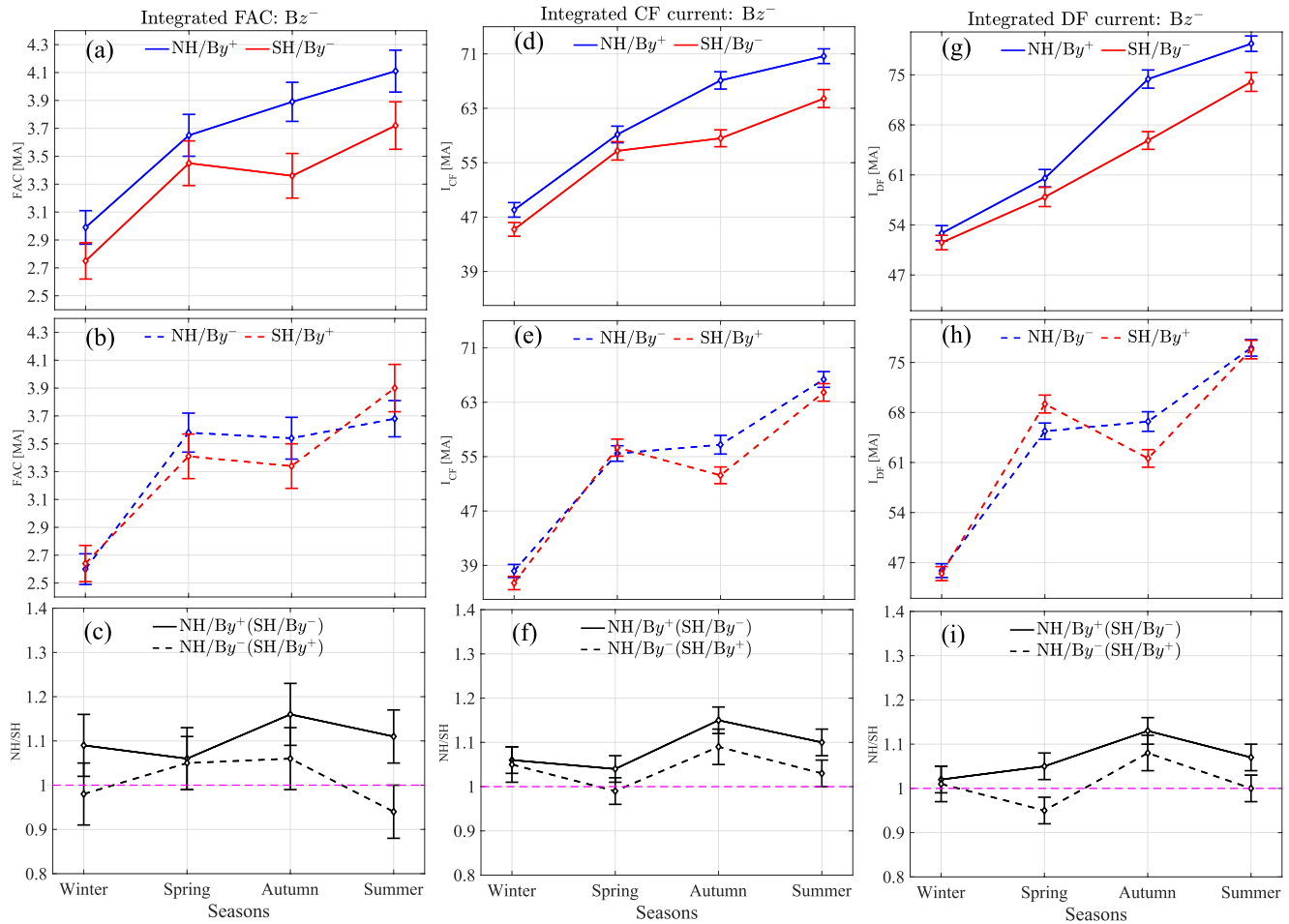


**Figure 8.** Same format as Figure 7, but for interplanetary magnetic field  $B_z^-$ .

Figure 8c shows the seasonal variation of the median NH/SH ratios of FACs obtained from bootstrapping for opposite IMF  $B_y$  directions in the two hemispheres during IMF  $B_z^-$  conditions. When  $B_y$  is positive in NH (solid line), statistically significant hemispheric asymmetry in FAC occurs in local winter, autumn and summer, with NH/SH ratios (see Table 2b)  $1.09 \pm 0.07$ ,  $1.16 \pm 0.07$  and  $1.11 \pm 0.06$ , respectively. When  $B_y$  is negative in NH (dashed line), the two hemispheres are statistically symmetric during all local seasons, at the 90% confidence level.

Figures 8d–8f and 8g–8i show the seasonal variation of integrated CF and DF currents, respectively, in the same format as FAC. Overall, the seasonal variation patterns are very similar to each other and to the FAC. The largest hemispheric asymmetry in both CF and DF currents occur in local autumn for  $B_y^+$  in the NH ( $B_y^-$  in the SH), when the NH/SH ratios are  $1.15 \pm 0.03$  for CF current (see Figure 8f and Table 2b) and  $1.13 \pm 0.04$  for DF current (see Figure 8g and Table 2b).

Overall, the difference in hemispheric current intensities is smaller during IMF  $B_z^-$  (Figures 8c, 8f and 8i) than during IMF  $B_z^+$  (Figures 7c, 7f and 7i). This is consistent with Paper II, where it was found that the hemispheric asymmetry is larger during low than high Kp conditions. Moreover, in each hemisphere, the IMF  $B_y$  effect on the integrated currents is larger during IMF  $B_z^+$  (Figure 7) than during IMF  $B_z^-$  (Figure 8).



#### 4. Cross Polar Cap Potential From SuperDARN Dynamic Model

The FACs and ionospheric horizontal currents are closely related to the electric field imposed on the ionosphere by the ionosphere-magnetosphere coupling. In Paper II, we have speculated that an external forcing related to hemispherically asymmetric convection electric field and/or particle precipitation may play a role on the hemispheric asymmetry in the auroral current systems.

The ionospheric convection electric field is commonly expressed in terms of the cross polar cap potential difference (CPCP) or patterns of plasma convection velocity (e.g., Cousins & Shepherd, 2010; Juusola et al., 2014; Pettigrew et al., 2010; Thomas & Shepherd, 2018). The cross polar cap potential have been calculated from measurements by satellites and ground based radars such as the SuperDARN. Several statistical models of high latitude plasma convection have been developed using SuperDARN radar data (e.g., Cousins & Shepherd, 2010; Pettigrew et al., 2010; Ruohoniemi & Greenwald, 1996, 2005; Thomas & Shepherd, 2018).

In this study, the SuperDARN Dynamical Model (SDDM) of high latitude plasma convection is used to calculate the cross polar cap potential difference and the plasma drift velocity for different seasons and IMF clock angle sectors. SDDM is based on Cousins and Shepherd (2010) convection model coefficients, hereafter called the CS10 model, which is an expansion of the convection model by Pettigrew et al. (2010). The CS10 convection model is based on 8 years of measurements from nine northern and six southern hemisphere SuperDARN radars. Recently, several radars were added to the northern hemisphere SuperDARN offering improved coverage at mid-latitudes and in the polar cap region (Thomas & Shepherd, 2018). However, the radar coverage in the southern hemisphere has not significantly changed since the CS10 model. Thus, the SDDM is the best tool for hemispheric comparison of the convection, as the difference between the hemispheres in the number of radars used for this model was not as large as it is now.

In addition to the relative sparsity of radar coverage in the SH, the radar fields-of-view in both hemispheres are concentrated toward the polar cap region (see Figure 1 in Pettigrew et al., 2010). This configuration is not ideal during strong IMF  $B_z^-$ , as the oval and convection cells expand equatorward and may not be covered by SH radars. Because of this situation, we calculate the CPCP values for each local season only during IMF  $B_z^+$  for both signs of IMF  $B_y$  in NH and SH. In the SDDM the seasonal effects are parameterize by dipole tilt angle values. We use  $+15^\circ$  dipole tilt for summer,  $-15^\circ$  for winter and  $0^\circ$  for equinoxes (spring and autumn). As input to the SDDM, we take the values of IMF  $B_z^+$  and solar wind velocity from their corresponding bootstrapped distributions, namely  $+2.0$  nT for  $B_z$  and  $400$  km/s for the velocity. We repeat the calculation for IMF  $B_y$  values in the range  $(-6, 6)$  nT with  $1$  nT steps. During each local season, the NH/SH ratios of CPCP are calculated for equal magnitudes but opposite IMF  $B_y$  signs between the two hemispheres.

Figures 9a and 9b, respectively, show the CPCP as a function of IMF  $B_y$  in NH and in SH for different local seasons during IMF  $B_z^+$ . In both hemispheres, the CPCP values increase as the magnitude of IMF  $B_y$  increases. However, there is a clear difference in the seasonal CPCP pattern as a function of  $B_y$  in each hemisphere. In NH, the local seasons are more similar to each other for IMF  $B_y^+$  (solid lines) than for IMF  $B_y^-$  (dashed lines), while the opposite is true in SH. For IMF  $B_y^-$  in the NH and IMF  $B_y^+$  in the SH, the CPCP values on average are largest in local summer, intermediate in equinox and smallest in local winter. Larger CPCP in local summer than in local winter was reported also in previous studies (e.g., Pettigrew et al., 2010; Ruohoniemi & Greenwald, 2005).

Figure 9c shows the NH/SH ratios of CPCP for opposite IMF  $B_y$  plotted as a function of IMF  $B_y$  values in NH. Dashed and solid lines are NH/SH ratios of dashed and solid lines from Figures 9a and 9b. The ratios indicate that the CPCP values are larger in NH than in SH. Overall, the hemispheric difference is larger for IMF  $B_y^-$  in the NH ( $B_y^+$  in the SH) than vice versa.

Figures 10a and 10b, respectively, show the NH/SH ratios of CPCP and DF current for opposite IMF  $B_y$  as a function of seasons. As the SDDM uses the dipole tilt angle to represent seasonal variations, the CPCP in local autumn and local spring are always equal. In Figure 10a, the CPCP ratios in each local season are obtained by averaging the ratios shown in Figure 9c over all values of IMF  $B_y$  for each sign separately. During local winter, the NH/SH ratio of CPCP is larger than 1 for both signs of IMF  $B_y$  in NH, which is in agreement with the NH/SH ratio of DF current, but the CPCP NH/SH ratios are smaller than the DF NH/SH ratios. However, unlike the DF current, the largest hemispheric difference in CPCP occurs in local summer

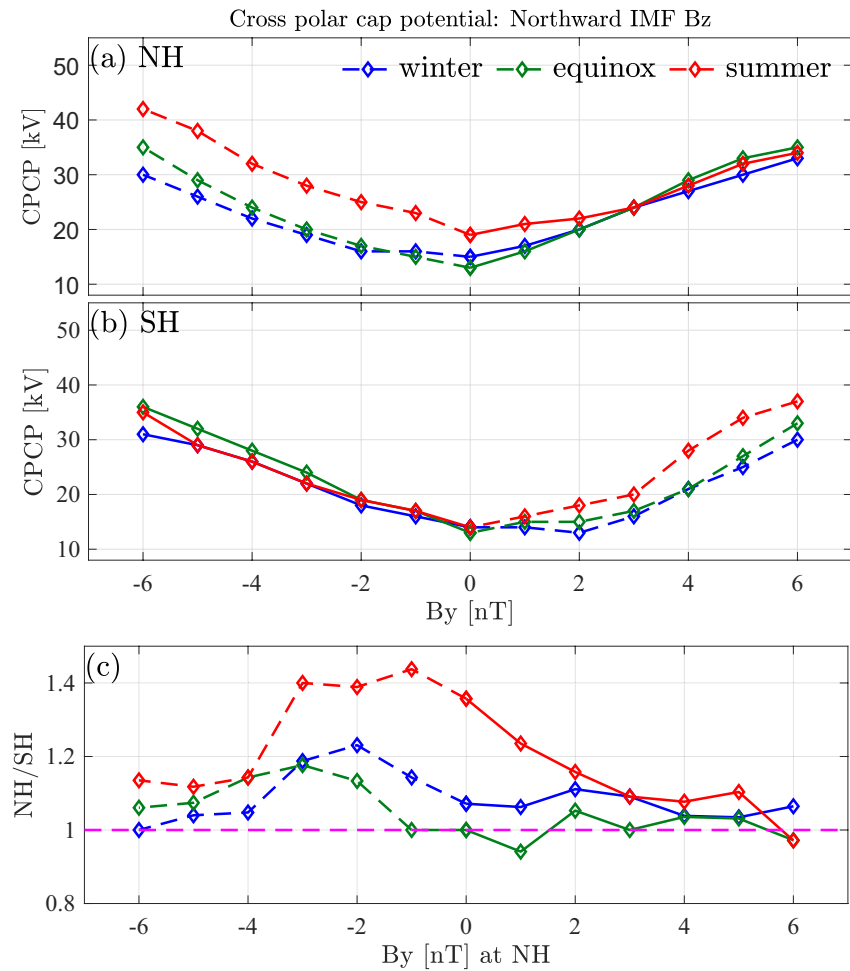


**Figure 9.** Cross polar cap potential difference as a function of interplanetary magnetic field (IMF)  $B_y$  in Northern Hemisphere (NH) (a) and in Southern Hemisphere (SH) (b) during IMF  $B_z^+$  for different local seasons. Panel (c) shows the NH/SH ratios of cross polar cap potential for opposite signs of IMF  $B_y$ : solid and dashed lines are for IMF  $B_y^+$  and for IMF  $B_y^-$  conditions in the NH, respectively. The horizontal axis shows the values of IMF  $B_y$  in NH.

for IMF  $B_y^-$  conditions in the NH. For all local seasons, the average NH/SH ratios of CPCP are larger for IMF  $B_y^-$  conditions in the NH than vice versa. In contrast, for most seasons, larger hemispheric asymmetry in the DF current occurs for IMF  $B_y^+$  conditions in the NH than vice versa. In fact, in Figure 10a the dashed line is always above the solid line and vice versa in Figure 10b (except in winter).

Next, we move to discuss the explicit  $B_y$  effect in a given hemisphere for CPCP values. Table 3 shows the CPCP ratios for  $B_y^+/B_y^-$  in the NH and  $B_y^-/B_y^+$  in the SH during both IMF  $B_z$  conditions. In both hemispheres, the largest  $B_y$  effect on CPCP occurs in local winter and equinox during IMF  $B_z^+$  conditions, when the CPCP values are 13%–24% larger for IMF  $B_y^+$  in NH and IMF  $B_y^-$  in SH than vice versa. In NH summer, CPCP value is larger for  $B_y^-$  than vice versa, while in SH summer the  $B_y$  effect is not statistically significant. Similar IMF  $B_y$  effect is visible also during IMF  $B_z^-$  conditions, but the effect is smaller, with the maximum enhancement of 8% in SH equinox.

Figure 11 presents the ratios of CPCP (same as Table 3) and DF current (data from Table 1) for opposite IMF  $B_y$  in each hemisphere. Here, we compare the effect of  $B_y$  on CPCP with DF current, which can be assumed to represent the auroral electrojets. As the SDDM uses the dipole tilt angle to represent seasonal variations, the CPCP in local autumn and local spring are always equal. Therefore, we have combined the DF current statistics from spring and autumn. During IMF  $B_z^+$ , the explicit  $B_y$  effect on CPCP and DF current is similar in winter and equinox for NH (Figure 11a), and in winter and summer for SH (Figure 11b). During IMF  $B_z^-$ ,

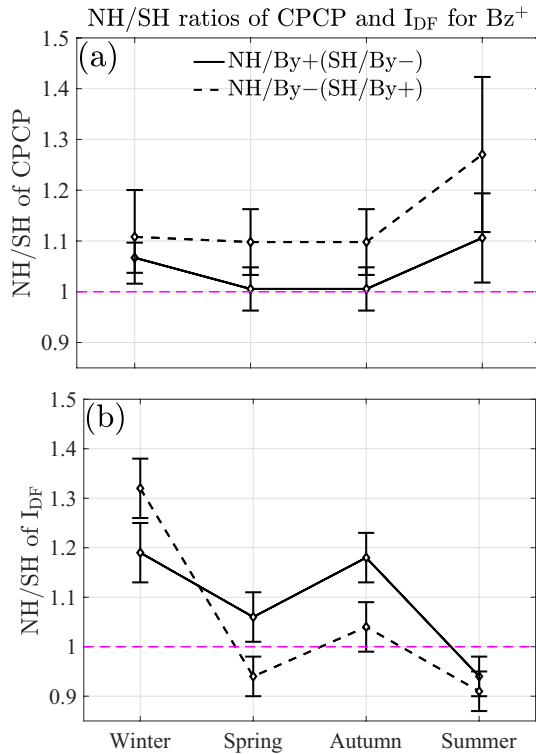


**Figure 10.** (a) Northern Hemisphere (NH)/Southern Hemisphere (SH) ratios of cross polar cap potential (CPCP) averaged over all interplanetary magnetic field (IMF)  $B_y^+$  conditions in the NH (solid line) or IMF  $B_y^-$  conditions in the NH (dashed line) as a function of season. The error bars are standard deviations, which are calculated for each IMF  $B_y$  sign separately using the six values in the range  $(\pm 1, \pm 6)$  nT, and thus show the variability of CPCP due to variability in the IMF  $B_y$  values. (b) Median NH/SH ratios of DF current (same as Figure 7i).

in NH the seasonal behavior is rather similar both for CPCP and DF (Figure 11c), but in SH the pattern is not very clear (Figure 11d). Altogether, the ratios for  $B_z^-$  are smaller than for  $B_z^+$ . Largest differences occur during equinoxes in SH for both signs of  $B_z$ , but we should keep in mind that the SDDM doesn't make a difference between spring and autumn. In both hemispheres, the maximum  $B_y$  effect on both CPCP and DF current occurs in local winter during IMF  $B_z^+$  conditions, when both the CPCP and DF current  $B_y^+/B_y^-$  ratios are about 1.18 in NH and  $B_y^-/B_y^+$  ratios are about 1.20–1.30 in SH. Overall, the results indicate that the effect of  $B_y$  on DF current is in very good agreement with the SuperDARN dynamic model CPCP during IMF  $B_z^+$  in winter for both hemispheres, at equinox for NH and in summer for SH.

When using the CPCP values and comparing them to the DF current as shown in Figures 10 and 11, one should keep in mind that there are some uncertainties and limitations in the SDDM model. As discussed before, the radar coverage in the SH is more limited than in the NH. Furthermore, the amount of data used to derive the CS10 coefficient can be rather limited for extreme values of the dipole tilt angle and large solar wind driving conditions. However, in our case the largest solar wind electric field used as input to the SDDM model is 2.5 mV/m, so our model values do not correspond to any extreme conditions and statistics are sufficient (see Figure 2 in Cousins & Shepherd, 2010).

## 5. Summary, Discussion, and Conclusions

In this paper, we have investigated the effect of the IMF on the hemispheric asymmetry in auroral currents measured by the Swarm satellites. The SECS method is used to estimate the FAC as well as the CF and DF parts of the ionospheric horizontal currents from nearly 6 years of Swarm vector magnetic field measurements. The data is divided into seasons and four IMF sectors based on the signs of the IMF  $B_z$  and  $B_y$ . In order to make the seasons and IMF  $B_y$  sectors comparable, bootstrap resampling technique is used to remove hemispheric and seasonal bias in the number of samples and in the Newell universal coupling function distributions.

We calculate the integrated FAC and average CF and DF currents for different seasons and IMF sectors, and the corresponding NH/SH ratios. The two hemispheres are compared under opposite IMF  $B_y$  signs. We also study the effect of the IMF  $B_y$  sign in a given hemisphere. Finally, in order to study the role of electric field in the hemispheric asymmetry of the auroral currents, we calculate the CPCP values using the SuperDARN dynamic model for both signs of IMF  $B_y$  during IMF  $B_z^+$  only, because the coverage of the radars in the SH does not extend to as low latitudes as in the NH, which is likely important for IMF  $B_z^-$  conditions.

**Table 3**

Ratios of CPCP for Opposite IMF  $B_y$  Directions in Each Hemisphere:  $B_y^+/B_y^-$  in NH and  $B_y^-/B_y^+$  in SH

CPCP ratios for opposite IMF $B_y$ directions: $B_y^+/B_y^-$ in NH, $B_y^-/B_y^+$ in SH				
IMF	Hemisphere	Winter	Equinox	Summer
$B_z^+$	NH	$1.18 \pm 0.08$	$1.13 \pm 0.08$	$0.86 \pm 0.04$
	SH	$1.22 \pm 0.14$	$1.24 \pm 0.12$	$0.99 \pm 0.09$
$B_z^-$	NH	$1.05 \pm 0.02$	$0.98 \pm 0.03$	$0.89 \pm 0.05$
	SH	$1.02 \pm 0.04$	$1.08 \pm 0.06$	$0.99 \pm 0.06$

Note. CPCP, cross polar cap potential; IMF, interplanetary magnetic field; NH, Northern Hemisphere; SH, Southern Hemisphere.



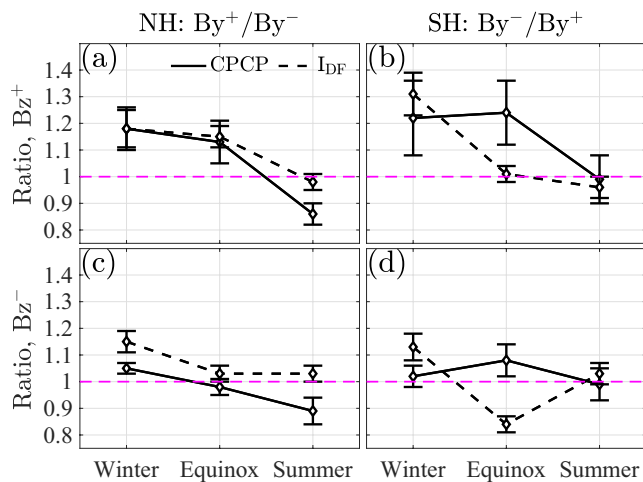


**Figure 11.** Ratios of cross polar cap potential (solid line) and DF current (dashed line) for opposite interplanetary magnetic field (IMF) By directions in Northern Hemisphere (a, c) and in Southern Hemisphere (b, d) during IMF Bz<sup>+</sup> (a, b) and Bz<sup>-</sup> (c, d) conditions.

The most important findings of this study are the following:

1. The hemispheric asymmetry in auroral currents is larger during Bz<sup>+</sup> (northward) than Bz<sup>-</sup> (southward) IMF conditions in local winter, irrespective of the IMF By sign. This is in line with previous result in Paper II, where we observed the strongest asymmetry in local winter during low Kp conditions.
2. For By<sup>+</sup> in the NH (By<sup>-</sup> in the SH), on average FACs as well as ionospheric horizontal currents are stronger in the NH than in the SH in most local seasons under both signs of IMF Bz. For IMF By<sup>-</sup> in the NH (By<sup>+</sup> in the SH), the hemispheric differences of auroral currents are small except in local winter.
3. During Bz<sup>+</sup> and By<sup>+</sup> in the NH (Bz<sup>+</sup> and By<sup>-</sup> in the SH), hemispheric asymmetry in auroral currents is largest in local winter and local autumn, and smallest in local summer. The NH/SH ratio for FACs in winter and autumn are  $1.18 \pm 0.09$  and  $1.17 \pm 0.09$ , respectively.
4. During Bz<sup>-</sup> and By<sup>+</sup> in the NH (Bz<sup>-</sup> and By<sup>-</sup> in the SH), hemispheric asymmetry in auroral currents is largest in local autumn for these IMF conditions. The NH/SH ratio for FAC, CF current and DF current in local autumn are  $1.16 \pm 0.07$ ,  $1.15 \pm 0.03$  and  $1.13 \pm 0.03$ , respectively.
5. Generally, in NH By<sup>+</sup> causes larger horizontal currents and FACs than By<sup>-</sup>. This explicit By effect is stronger for Bz<sup>+</sup> (northward) than Bz<sup>-</sup> (southward) IMF. For Bz<sup>+</sup>, the By effect is statistically significant in Autumn (strongest) and Winter, for Bz<sup>-</sup> in Autumn (strongest), Winter and Summer (weakest). The effect is not seen in the NH Spring. SH has a corresponding behavior for reversed By signs, but the effect is weaker in the SH, so generally it is seen only in Autumn and Winter.
6. The explicit By effect in a given hemisphere for currents can tentatively be explained by the SuperDARN dynamic model CPCP for IMF Bz<sup>+</sup> in winter for both hemispheres, at equinox for NH and in summer for SH. Hence, in winter both the DF current and CPCP By<sup>+</sup>/By<sup>-</sup> ratios are about 1.18 in NH and By<sup>-</sup>/By<sup>+</sup> ratios are about 1.2–1.3 in SH.
7. However, when the hemispheric asymmetry is studied using the SuperDARN dynamic model, the CPCP NH/SH ratios for IMF Bz<sup>+</sup> do not, in general, agree with the behavior of auroral current ratios. Only in winter, both the CPCP and auroral currents show NH/SH ratios over 1 for both signs of IMF By. Furthermore, during IMF Bz<sup>+</sup> the highest NH/SH value of 1.27 in CPCP is obtained for summer, while for auroral currents the value is below 1.0 during summer.

In addition to the convective electric field, the magnitude of currents in the auroral ionosphere depends on auroral conductance due to particle precipitation. In Paper II, we studied the role of background conductances using IRI, CHAOS and MSISE models that include effects of solar illumination, magnetic field structure and neutral atmosphere properties, respectively. We found that background conductances do not explain the hemispheric asymmetry in currents. The calculation based on IRI electron density did not show the auroral oval, so the role of precipitation induced conductances could not be investigated. Using Swarm A magnetic and electric field measurements, Ivarsen et al. (2020) found a larger Alfvén wave reflection coefficient in the NH than in the SH. They interpreted this observation as a consequence of hemispheric asymmetry in the precipitation induced conductance, with the largest hemispheric asymmetry seen during local winter. This result is in line with the hemispheric asymmetry in the auroral currents observed in this study as well as in Paper II. Therefore, the occurrence of stronger auroral currents in the NH than in the SH during local winter might be explained by a hemispherically asymmetric particle precipitation.

Furthermore, Coxon et al. (2016) found an asymmetry in the FAC magnitudes in the two hemispheres and noted that the difference between the two hemispheres is larger during larger dayside reconnection rates. They speculated that this could be an effect of asymmetry in the Earth's magnetic field or an effect

of asymmetry in the total electron content in the two hemispheres. This is in contrast to our results, as in the present study the strongest asymmetries are seen during IMF  $B_z^+$ , and in Paper II we concluded that the solar induced background conductances could not explain the observed asymmetries. In the case of substorms occurring during IMF  $B_y \neq 0$  conditions, Ohma et al. (2018) reported that the hemispheric asymmetry in conjugate auroral features decreases during the expansion phase. They attribute this effect to the increased reconnection rate in the magnetotail, which reduces the asymmetric lobe pressure created by IMF  $B_y$ . They further note that if the substorms and tail reconnection are the key factors removing the hemispheric asymmetries, then the asymmetry should be largest during northward IMF  $B_z$  and slow solar wind velocities, when the substorm rate is low. This scenario is in qualitative agreement with the results reported in this study, and also in Papers I and II, where the asymmetry was found to be largest during low Kp conditions. The agreement suggests that the role of IMF  $B_y$  in producing hemispheric asymmetry, and the role of tail reconnection in decreasing the asymmetry, should be further investigated.

Regarding the explicit IMF  $B_y$  effect in a given hemisphere, our results are in agreement with several other previous studies (e.g., Holappa & Mursula, 2018; Holappa et al., 2020, 2021; Laundal et al., 2018; Ohma et al., 2021; Smith et al., 2017, references therein). Using satellite measurements, Smith et al. (2017) found larger auroral electrojet current in the NH winter for IMF  $B_y^+$  and in the SH winter for IMF  $B_y^-$  than vice versa. Laundal et al. (2018) reported a similar explicit IMF  $B_y$  effect on FACs and DF currents using the Average Magnetic field and Polar current System (AMPS) model in the NH winter. Using FAC measurements from AMPERE, Holappa et al. (2021) found stronger R1 and R2 FACs for  $B_y^+$  than for  $B_y^-$  in the NH winter, and for  $B_y^-$  than for  $B_y^+$  in the SH winter for the same level of solar wind driving. Ohma et al. (2021) reported more frequent substorm occurrence rate when  $B_y$  and the dipole tilt angle have different signs as opposed to when they have the same signs. Results in the above studies are in line with the results reported in this study (see Table 1), where FAC, CF, and DF current in NH winter and spring are larger for IMF  $B_y^+$  than for IMF  $B_y^-$ . Our results also show similar IMF  $B_y$  dependence of FAC, CF, and DF currents in the SH, but for opposite polarity of IMF  $B_y$ .

The physical mechanism of the explicit  $B_y$  effect on the high latitude ionospheric currents is not yet known. However, recent studies suggest that this effect is likely to be associated with the “penetration” of the IMF  $B_y$  component into the closed magnetosphere (e.g., Østgaard et al., 2015) and changes in the solar wind-magnetosphere coupling due to IMF  $B_y$  signs (e.g., Reistad et al., 2020). Reistad et al. (2020) found that during NH winter (SH summer), on average the polar cap is larger for IMF  $B_y^+$  than IMF  $B_y^-$ . This explicit IMF  $B_y$  effect is found to reverse during NH summer (SH winter). They interpret the different responses of the polar cap size due to the sign of IMF  $B_y$  to likely be a result of differences in the dayside reconnection rate. The larger dayside reconnection rate is expected to correspond to a larger CPCP, which is in accordance with the findings in this study.

Our statistical results indicate the presence of spring-autumn asymmetry in currents (see Figure 7). In Section 3.3, we mention that the observed spring-autumn asymmetry in currents may be related to the RM effect of Russell and McPherron (1973) and the axial effect discussed by Mursula et al. (2011). We note that in principle the bootstrapping procedure with the Newell coupling function should remove both the RM effect and the axial effect, assuming that the 30 min averaging of the coupling function used in this study is long enough. However, if there are some residual effects or memory in the magnetosphere for periods longer than this, the RM effect and the axial effect could make some contribution to the observed spring-fall asymmetry.

The factors causing the observed hemispheric asymmetries in the auroral currents are still unclear. The CPCP values from the SuperDARN dynamic model shown in this study suggest that the convection electric field cannot fully explain the hemispheric asymmetry in auroral currents. Furthermore, in Paper II we have concluded that local background conductances calculated with the IRI model cannot explain the asymmetry either. However, the role of precipitation induced conductivities remains unclear, and should be further investigated using available measurements and numerical simulation of the magnetosphere and magnetosphere-ionosphere coupling. At the same time, as discussed above, the role of IMF  $B_y$  related tail reconnection in producing and removing hemispheric asymmetry in the magnetotail and in the ionospheric currents merits closer study, for example by comparing our statistical results with the output of global simulations of the coupled solar wind-magnetosphere-ionosphere system.

## Data Availability Statement

The calibrated 1 Hz Swarm magnetic field data are available at <https://swarm-diss.eo.esa.int>. The OMNI data were obtained from NASA/GSFC's Space Physics Data Facility's OMNIWeb at <http://omniweb.gsfc.nasa.gov>. The CHAOS model (CHAOS-6-x8 and CHAOS-7) is available at <http://www.spacecenter.dk/files/magnetic-models/CHAOS-6>. The SuperDARN dynamic model is available at <http://sdnet.thayer.dartmouth.edu/models/dynamicmodel.php#SDDM>.

## Acknowledgments

This work was supported by the Academy of Finland (project 314664) and support for S. G. Shepherd provided by National Science Foundation (grant AGS-1934997). The European Space Agency (ESA) is acknowledged for providing the Swarm data. SuperDARN is a collection of radars funded by national scientific funding agencies of Australia, Canada, China, France, Italy, Japan, Norway, South Africa, United Kingdom, and the United States of America. The Altitude adjusted corrected geomagnetic (AACGM) coordinate transformation software is available at <http://superdarn.thayer.dartmouth.edu/aacgm.html>. The authors greatly appreciate the availability of the software from these websites.

## References

- Amm, O., Vanhamäki, H., Kauristie, K., Stolle, C., Christiansen, F., Haugmans, R., et al. (2015). A method to derive maps of ionospheric conductances, currents, and convection from the Swarm multisatellite mission. *Journal of Geophysical Research: Space Physics*, 120(4), 3263–3282. <https://doi.org/10.1002/2014JA020154>
- Burke, W. J., & Doyle, M. A. (1986). Interplanetary control of high latitude electrodynamics. *Journal of Geomagnetism and Geoelectricity*, 38(11), 1115–1141. <https://doi.org/10.5636/jgg.38.1115>
- Chernick, M. R., & LaBudde, R. A. (2011). *An introduction to Bootstrap methods with applications to R*. Thomas Jefferson University, John Wiley and Sons, Inc. <https://www.wiley.com/en-us/exportProduct/pdf/9780470467046>
- Cousins, E. D. P., & Shepherd, S. G. (2010). A dynamical model of high-latitude convection derived from SuperDARN plasma drift measurements. *Journal of Geophysical Research*, 115(A12). <https://doi.org/10.1029/2010ja016017>
- Coxon, J. C., Milan, S. E., Carter, J. A., Clausen, L. B. N., Anderson, B. J., & Korth, H. (2016). Seasonal and diurnal variations in AMPERE observations of the birkeland currents compared to modeled results. *Journal of Geophysical Research: Space Physics*, 121(5), 4027–4040. <https://doi.org/10.1002/2015JA022050>
- Dekking, F. M., Kraaikamp, C., Lopenha, H., & Meester, L. (2005). *A modern introduction to probability and statistics*. Springer-Verlag London.
- Finlay, C. C., Olsen, N., Kotsiaros, S., Gillet, N., & Tøffner-Clausen, L. (2016). Recent geomagnetic secular variation from Swarm and ground observatories as estimated in the CHAOS-6 geomagnetic field model. *Earth, Planets and Space*, 68(1), 112. <https://doi.org/10.1186/s40623-016-0486-1>
- Green, D. L., Waters, C. L., Anderson, B. J., & Korth, H. (2009). Seasonal and interplanetary magnetic field dependence of the field-aligned currents for both Northern and Southern Hemispheres. *Annales Geophysicae*, 27(4), 1701–1715. <https://doi.org/10.5194/angeo-27-1701-2009>
- Haaland, S. E., Paschmann, G., Förster, M., Quinn, J. M., Torbert, R. B., McIlwain, C. E., et al. (2007). High-latitude plasma convection from cluster EDI measurements: Method and IMF-dependence. *Annales Geophysicae*, 25(1), 239–253. <https://doi.org/10.5194/angeo-25-239-2007>
- Holappa, L., Asikainen, T., & Mursula, K. (2020). Explicit IMF dependence in geomagnetic activity: Modulation of precipitating electrons. *Geophysical Research Letters*, 47(4), e2019GL086676. <https://doi.org/10.1029/2019GL086676>
- Holappa, L., & Mursula, K. (2018). Explicit IMF by dependence in high-latitude geomagnetic activity. *Journal of Geophysical Research: Space Physics*, 123(6), 4728–4740. <https://doi.org/10.1029/2018ja025517>
- Holappa, L., Robinson, R. M., Pulkkinen, A., Asikainen, T., & Mursula, K. (2021). Explicit IMF by-dependence in geomagnetic activity: Quantifying ionospheric electrodynamics. *Journal of Geophysical Research: Space Physics*, 126(4), e2021JA029202. <https://doi.org/10.1029/2021JA029202>
- Huang, Tao., Lühr, H., & Wang, H. (2017). Global characteristics of auroral Hall currents derived from the Swarm constellation: dependences on season and IMF orientation. *Annales Geophysicae*, 35(6), 1249–1268. <https://doi.org/10.5194/angeo-35-1249-2017>
- Ivarsen, M. F., Park, J., Kwak, Y.-S., Jin, Y., Knudsen, D. J., & Clausen, L. B. N. (2020). Observational evidence for the role of hall conductance in alfvén wave reflection. *Journal of Geophysical Research: Space Physics*, 125(12), e2020JA028119. <https://doi.org/10.1029/2020JA028119>
- Juusola, L., Kauristie, K., Vanhamäki, H., Aikio, A., & van de Kamp, M. (2016). Comparison of auroral ionospheric and field-aligned currents derived from Swarm and ground magnetic field measurements. *Journal of Geophysical Research: Space Physics*, 121(9), 9256–9283. <https://doi.org/10.1002/2016JA022961>
- Juusola, L., Milan, S. E., Lester, M., Grocott, A., & Imber, M. S. (2014). Interplanetary magnetic field control of the ionospheric field-aligned current and convection distributions. *Journal of Geophysical Research: Space Physics*, 119(4), 3130–3149. <https://doi.org/10.1002/2013ja019455>
- Laundal, K. M., Cnossen, I., Milan, S. E., Haaland, S. E., Coxon, J., Pedatella, N. M., et al. (2017). North–South asymmetries in Earth's magnetic field. *Space Science Reviews*, 206(1–4), 225–257. <https://doi.org/10.1007/s11214-016-0273-0>
- Laundal, K. M., Finlay, C. C., & Olsen, N. (2016). Sunlight effects on the 3D polar current system determined from low Earth orbit measurements. *Earth, Planets and Space*, 68(1), 142. <https://doi.org/10.1186/s40623-016-0518-x>
- Laundal, K. M., Finlay, C. C., Olsen, N., & Reistad, J. P. (2018). Solar wind and seasonal influence on ionospheric currents from Swarm and CHAMP measurements. *Journal of Geophysical Research: Space Physics*, 123(5), 4402–4429. <https://doi.org/10.1029/2018ja025387>
- Liou, K., Sotirelis, T., & Mitchell, E. (2020). Control of the east-west component of the interplanetary magnetic field on the occurrence of magnetic substorms. *Geophysical Research Letters*, 47(5), e2020GL087406. <https://doi.org/10.1029/2020GL087406>
- Lockwood, M., Owens, M. J., Barnard, L. A., Haines, C., Scott, C. J., McWilliams, K. A., & Coxon, J. C. (2020). Semi-annual, annual and universal time variations in the magnetosphere and in geomagnetic activity: 1. geomagnetic data. *Journal of Space Weather and Space Climate*, 10, 23. <https://doi.org/10.1051/swsc/2020023>
- Milan, S. E., Clausen, L. B. N., Coxon, J. C., Carter, J. A., Walach, M. T., Laundal, K., et al. (2017). Overview of solar wind–magnetosphere–ionosphere–atmosphere coupling and the generation of magnetospheric currents. *Space Science Reviews*, 206(1–4), 547–573. <https://doi.org/10.1007/s11214-017-0333-0>
- Mursula, K., Tanskanen, E., & Love, J. J. (2011). Spring-fall asymmetry of substorm strength, geomagnetic activity and solar wind: Implications for semiannual variation and solar hemispheric asymmetry. *Geophysical Research Letters*, 38(6). <https://doi.org/10.1029/2011gl046751>
- Newell, P. T., Sotirelis, T., Liou, K., Meng, C.-I., & Rich, F. J. (2007). A nearly universal solar wind-magnetosphere coupling function inferred from 10 magnetospheric state variables. *Journal of Geophysical Research*, 112(A1). <https://doi.org/10.1029/2006ja012015>



- Ohma, A., Østgaard, N., Reistad, J. P., Tenfjord, P., Laundal, K. M., Snekvik, K., et al. (2018). Evolution of asymmetrically displaced footpoints during substorms. *Journal of Geophysical Research: Space Physics*, 123(12), 10030–10063. <https://doi.org/10.1029/2018JA025869>
- Ohma, A., Reistad, J. P., & Hatch, S. M. (2021). Modulation of magnetospheric substorm frequency: Dipole tilt and IMF by effects. *Journal of Geophysical Research: Space Physics*, 126(3), e2020JA028856. <https://doi.org/10.1029/2020JA028856>
- Ohtani, S., Ueno, G., & Higuchi, T. (2005). Comparison of large-scale field-aligned currents under sunlit and dark ionospheric conditions. *Journal of Geophysical Research*, 110(A9). <https://doi.org/10.1029/2005ja011057>
- Østgaard, N., Reistad, J. P., Tenfjord, P., Laundal, K. M., Snekvik, K., Milan, S., & Haaland, S. (2015). Mechanisms that produce auroral asymmetries in conjugate hemispheres. In *Auroral dynamics and space weather* (pp. 131–143). American Geophysical Union (AGU). <https://doi.org/10.1002/9781118978719.ch10>
- Pakhotin, I. P., Mann, I. R., Xie, K., Burchill, J. K., & Knudsen, D. J. (2021). Northern preference for terrestrial electromagnetic energy input from space weather. *Nature Communications*, 12(1), 199. <https://doi.org/10.1038/s41467-020-20450-3>
- Pettigrew, E. D., Shepherd, S. G., & Ruohoniemi, J. M. (2010). Climatological patterns of high-latitude convection in the northern and southern hemispheres: Dipole tilt dependencies and interhemispheric comparisons. *Journal of Geophysical Research*, 115(A7). <https://doi.org/10.1029/2009ja014956>
- Reistad, J. P., Laundal, K. M., Ohma, A., Moretto, T., & Milan, S. E. (2020). An explicit IMF b dependence on solar wind-magnetosphere coupling. *Geophysical Research Letters*, 47(1), e2019GL086062. <https://doi.org/10.1029/2019GL086062>
- Reistad, J. P., Østgaard, N., Laundal, K. M., Haaland, S., Tenfjord, P., Snekvik, K., et al. (2014). Intensity asymmetries in the dusk sector of the poleward auroral oval due to IMF Bx. *Journal of Geophysical Research: Space Physics*, 119(12), 9497–9507. <https://doi.org/10.1002/2014JA020216>
- Ruohoniemi, J. M., & Greenwald, R. A. (1996). Statistical patterns of high-latitude convection obtained from goose bay hf radar observations. *Journal of Geophysical Research*, 101(A10), 21743–21763. <https://doi.org/10.1029/96ja01584>
- Ruohoniemi, J. M., & Greenwald, R. A. (2005). Dependencies of high-latitude plasma convection: Consideration of interplanetary magnetic field, seasonal, and universal time factors in statistical patterns. *Journal of Geophysical Research*, 110(A9). <https://doi.org/10.1029/2004ja010815>
- Russell, C. T. (2000). The solar wind interaction with the Earth's magnetosphere: A tutorial. *IEEE Transactions on Plasma Science*, 28(6), 1818–1830. <https://doi.org/10.1109/27.902211>
- Russell, C. T., & McPherron, R. L. (1973). Semiannual variation of geomagnetic activity. *Journal of Geophysical Research*, 78(1), 92–108. <https://doi.org/10.1029/ja078i001p00092>
- Shepherd, S. G. (2014). Altitude-adjusted corrected geomagnetic coordinates: Definition and functional approximations. *Journal of Geophysical Research: Space Physics*, 119(9), 7501–7521. <https://doi.org/10.1002/2014JA020264>
- Smith, A. R. A., Beggan, C. D., Macmillan, S., & Whaler, K. A. (2017). Climatology of the auroral electrojets derived from the along-track gradient of magnetic field intensity measured by pogo, magsat, champ, and swarm. *Space Weather*, 15(10), 1257–1269. <https://doi.org/10.1002/2017sw001675>
- Thomas, E. G., & Shepherd, S. G. (2018). Statistical patterns of ionospheric convection derived from mid-latitude, high-latitude, and polar SuperDARN HF radar observations. *Journal of Geophysical Research: Space Physics*, 123(4), 3196–3216. <https://doi.org/10.1002/2018ja025280>
- Vanhamäki, H., Juusola, L., Kauristie, K., Workayehu, A., & Käkki, S. (2020). Spherical Elementary Current Systems Applied to Swarm Data. In: M. Dunlop & H. Lühr (Eds.), *Ionospheric Multi-Spacecraft Analysis Tools. ISSI Scientific Report Series* (Vol. 17). Springer, Cham. [https://doi.org/10.1007/978-3-030-26732-2\\_3](https://doi.org/10.1007/978-3-030-26732-2_3)
- Workayehu, A. B., Vanhamäki, H., & Aikio, A. T. (2019). Field-aligned and horizontal currents in the northern and southern hemispheres from the swarm satellite. *Journal of Geophysical Research: Space Physics*, 124(0). <https://doi.org/10.1029/2019ja026835>
- Workayehu, A. B., Vanhamäki, H., & Aikio, A. T. (2020). Seasonal effect on hemispheric asymmetry in ionospheric horizontal and field-aligned currents. *Journal of Geophysical Research: Space Physics*, 125(10), e2020JA028051. <https://doi.org/10.1029/2020JA028051>
- Zhao, H., & Zong, Q.-G. (2012). Seasonal and diurnal variation of geomagnetic activity: Russell-mcpherron effect during different IMF polarity and/or extreme solar wind conditions. *Journal of Geophysical Research: Space Physics*, 117(A11). <https://doi.org/10.1029/2012ja017845>